Dysregulated *H19/Igf2* expression disrupts cardiac-placental axis during development of Silver Russell Syndrome-like mouse models

Suhee Chang[1], Diana Fulmer[1,2], Stella K. Hur[1], Joanne L. Thorvaldsen[1], Li Li[1,2], Yemin Lan[1], Eric A. Rhon-Calderon[1], Xiaowen Chen[2], Jonathan A. Epstein[1,2], Marisa S. Bartolomei[1]

[1]Department of Cell and Developmental Biology, Epigenetics Institute, Perelman School of Medicine, University of Pennsylvania, Philadelphia, PA, United States

[2]Penn Cardiovascular Institute, Perelman School of Medicine, University of Pennsylvania, Philadelphia, PA, United States

[*Keywords*: *H19*; *Igf2*; SRS; cardiac development; cardiac-placental axis; VSD; ECM; endothelial cells]

Corresponding author: bartolom@pennmedicine.upenn.edu

Abstract

Dysregulation of the imprinted *H19/IGF2* locus can lead to Silver-Russell Syndrome (SRS) in humans. However, the mechanism of how abnormal *H19/IGF2* expression contributes to various SRS phenotypes remains unclear, largely due to incomplete understanding of the developmental functions of these two genes. We previously generated a mouse model with humanized *H19/IGF2* ICR (*hIC1*) on the paternal allele that exhibited *H19/Igf2* dysregulation together with SRS-like growth restriction and perinatal lethality. Here we dissect the role of *H19* and *Igf2* in cardiac and placental development utilizing multiple mouse models with varying levels of *H19* and *Igf2*. We report severe cardiac defects such as ventricular septal defects (VSDs) and thinned myocardium, placental anomalies including thrombosis and vascular malformations, together with growth restriction in mouse embryos that correlated with the extent of *H19/Igf2* dysregulation. Transcriptomic analysis using cardiac endothelial cells of these mouse models shows that *H19/Igf2* dysregulation disrupts pathways related to extracellular matrix (ECM) and proliferation of endothelial cells. Our work links the heart and placenta through regulation by *H19* and *Igf2*, demonstrating that accurate dosage of both *H19* and *Igf2* is critical for normal embryonic development, especially related to the cardiac-placental axis.

Introduction

Genomic imprinting is a mammalian-specific phenomenon where a small number of genes are expressed in an allele-specific manner. Functionally, imprinted genes have central roles in development and growth in both humans and mice (Barlow & Bartolomei, 2014). Additionally, proper gene dosage of most imprinted genes is essential for normal development. Human chromosome 11 and the orthologous region on mouse chromosome 7 harbor two jointly controlled growth regulators with opposing functions; *H19* long noncoding RNA (lncRNA) and Insulin-like Growth Factor 2 (*IGF2/Igf2).* These two imprinted genes share an imprinting control region (ICR), a *cis*-regulatory element located between two genes, which is essential for their allele-specific expression, as well as tissue-specific enhancers located

40 downstream of *H19* (Chang & Bartolomei, 2020). The *H19/IGF2* ICR, which is designated as IC1 in
41 humans, binds CTCF on the maternal allele, forming an insulator and enabling *H19* exclusive access to
42 the shared enhancers (Figure 1A). On the paternal allele, the *H19/IGF2* ICR is methylated, which
43 prevents CTCF from binding and an insulator from forming. Consequently, *IGF2* usurps the shared
44 enhancers and *H19* is repressed on the paternal allele. Ultimately, allele-specific ICR methylation
45 facilitates monoallelic expression of *H19* and *IGF2* with *H19* expressed from the maternal allele and
46 *IGF2* expressed from the paternal allele.

47 Dysregulation of the *H19/IGF2* cluster is associated with two growth disorders, Beckwith-
48 Wiedemann Syndrome (BWS) and Silver-Russell Syndrome (SRS). In contrast to overgrowth observed
49 for BWS, SRS is characterized by intrauterine growth restriction resulting in small for gestational age
50 (SGA) births. Other symptoms of SRS vary widely among patients and include hemihypotrophy,
51 cognitive impairment, relative macrocephaly, and fifth-finger clinodactyly (Wakeling et al., 2017).
52 Approximately 50% of patients with SRS exhibit IC1 hypomethylation (Eggermann, Buiting, & Temple,
53 2011). Lack of methylation may allow the formation of an ectopic insulator on paternal IC1, which likely
54 explains why this class of SRS individuals has biallelic *H19* expression and greatly diminished *IGF2*
55 expression (Abi Habib et al., 2017; Gicquel et al., 2005). Importantly, ICR mutations in the mouse that
56 were generated to study imprinted gene regulation provided critical information suggesting a role for *H19*
57 and *IGF2* in SRS. For example, mutating CpGs at CTCF sites on the paternal *H19/Igf2* ICR resulted in
58 the loss of ICR methylation, activation of paternal *H19* and reduced *Igf2* expression (Engel, West,
59 Felsenfeld, & Bartolomei, 2004). This mutation led to restricted embryonic growth, which phenocopies
60 SRS. Nevertheless, although we and others successfully modeled a subset of SRS mutations in the mouse,
61 not all mutations were translatable because the mouse *H19*/*Igf2* ICR lacks extensive sequence
62 conservation with human IC1. Thus, a mouse model with human IC1 sequence substituted for the
63 endogenous mouse *H19*/*Igf2* ICR was generated ($H19^{hIC1}$, shortened as *hIC1*; Hur et al., 2016) to model
64 human mutations more precisely (Freschi et al., 2021, 2018). Consistent with expectations, maternally
65 transmitted *hIC1* successfully maintained insulator function, suggesting the possibility to model human

66 IC1 mutations endogenously in mice upon maternal transmission. In contrast, paternally transmitted *hIC1*
67 showed loss of methylation and formation of an ectopic insulator. Consequently, paternal *hIC1*
68 transmission caused elevated *H19* expression and *Igf2* depletion together with growth restriction and
69 embryonic lethality (Hur et al., 2016). Although the epigenetic defects and growth restriction of these
70 mice model SRS, the epigenetic defects in human are mosaic (Soellner et al., 2019), with a subset of cells
71 showing normal methylation patterns, providing a potential explanation for why SRS individuals are
72 viable.

73 The mechanism by which *H19/IGF2* expression dysregulation causes SRS phenotypes is
74 unknown, largely because the function of these two genes during development is incompletely
75 understood. *IGF2* is a well-described growth factor promoting fetoplacental growth, which functions in
76 an endocrine/paracrine manner through binding to IGF/Insulin receptors (Harris & Westwood, 2012).
77 Decreased *IGF2* levels in patients with SRS suggests that IGF2 contributes to restricted growth in these
78 patients (Abi Habib et al., 2017; Begemann et al., 2015; Gicquel et al., 2005). Consistently, in mice,
79 paternal-specific deletion of *Igf2* resulted in loss of *Igf2* expression and pre- and postnatal growth
80 restriction (DeChiara, Robertson, & Efstratiadis, 1991; Haley et al., 2012). In contrast, the exact role of
81 *H19* remains unclear. Previous studies in mouse suggested that *H19* lncRNA is a precursor for microRNA
82 (miR)-675, which regulates *Igf1r* expression (Keniry et al., 2012), and that *H19* represses *Igf2* expression
83 *in trans* (Gabory et al., 2009). As a result, *H19* has been largely overlooked and suggested to be an
84 occasional regulator of *Igf2* expression. Nevertheless, a previously described mouse model with *H19*
85 overexpression without changes in *Igf2* expression showed embryonic growth restriction (Drewell et al.,
86 2000), suggesting that *H19* mediates growth suppression independently from *Igf2*. Here, we report severe
87 developmental defects of the heart and placenta in mouse models with dysregulated *H19/Igf2* expression.
88 Embryos with the paternal *hIC1* showed atrioventricular (AV) cushion defects in the heart coupled with
89 ventricular septal defects (VSDs), and extremely thinned myocardial walls. Combined with placental
90 anomalies, the cardiac defects most likely contribute to the lethality of these mice (Kochilas, Li, Jin,
91 Buck, & Epstein, 1999; Snider & Conway, 2011). Normalization of *H19* rescued neither the lethality nor

growth restriction, although we observed a minimal rescue of the earlier growth and resorption frequency. Ultimately, modifying both *H19* and *Igf2* expression was necessary to rescue most phenotypes. Transcriptomic analysis of embryonic cardiac endothelial cells identified several key signaling pathways that are affected by the dysregulated *H19* and *Igf2,* and are potentially responsible for the paternal *hIC1*-related cardiac defects. This work emphasizes the importance of accurate dosage of *H19* and *Igf2* expression in normal cardiac and placental development, disruption of which can lead to SRS-like pathologies.

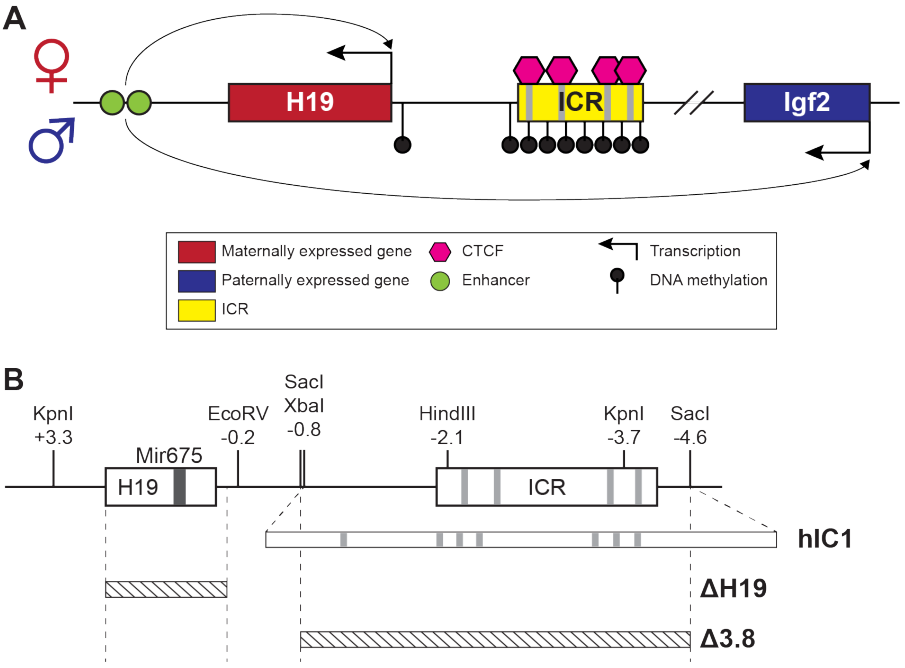

Figure 1. *H19/Igf2* cluster and mouse models utilized in this study.
(A) A schematic representation of the wild-type *H19/Igf2* cluster in mouse. The maternally-expressed *H19* and the paternally-expressed *Igf2* genes are shown in red and blue, respectively. Black lollipops on the paternal allele represent DNA methylation. The maternal ICR is bound to CTCF proteins (pink hexagons) at CTCF binding sites, forming an insulator that blocks the maternal *Igf2* promoter from the shared enhancers (green circles). These enhancers interact with the *H19* promoter on the maternal allele and *Igf2* promoter on the paternal allele. (B) Schematic of the mouse endogenous *H19/Igf2* ICR, $H19^{hIC1}$ (shortened as *hIC1*; Hur et al. 2016), $H19^{\Delta 2.8kb\text{-}H19}$ (shortened as *ΔH19*), and $H19^{\Delta 3.8kb\text{-}5'H19}$ (shortened as *Δ3.8*; Thorvaldsen et al. 2002, 2006) alleles. Restriction site locations (kb) are relative to the *H19* transcription start site. Gray lines on the ICR represent conserved CTCF binding sequences.

101 **Results**

102 Mouse models with genetic modifications that perturb *H19* and *Igf2* to different extents were used
103 to address the phenotypic consequences of abnormal *H19* and *Igf2* levels (Figure 1B). *hIC1* refers to the
104 humanized $H19^{hIC1}$ allele that substitutes the endogenous mouse *H19/Igf2* ICR with the corresponding
105 human IC1 sequence, which was initially generated to study human BWS and SRS mutations in the
106 mouse (Freschi et al., 2018; Hur et al., 2016). Paternal transmission of *hIC1* [*+/hIC1*] was previously
107 reported to increase *H19* and greatly diminish *Igf2* expression and resulted in embryonic lethality.
108

109 **Cardiac and placental defects in *+/hIC1* embryos**

110 Our initial experiments examined the developmental phenotype of *+/hIC1* embryos to determine
111 how abnormal *H19/Igf2* expression resulted in dramatic growth defects and lethality. As previously
112 reported (Hur et al., 2016), *+/hIC1* embryos showed severe growth restriction (note that for heterozygous
113 embryos, maternal allele is written first, Figure 2A). The growth restriction appeared as early as E11.5
114 and was greatly exaggerated by the end of gestation. Although E18.5 *+/hIC1* embryos were observed
115 alive and weighed approximately 40% of their wild-type littermates, *+/hIC1* neonates were perinatally
116 lethal, with no live pups found on the day of birth. To ascertain the source of lethality, we first examined
117 lungs from dead *+/hIC1* neonates. The lungs floated in water, demonstrating that *+/hIC1* pups respired
118 after birth (Borensztein et al., 2012). Additionally, *+/hIC1* neonates did not have a cleft palate, but no
119 milk spots were found, indicating a lack of feeding.

120 Histological analyses were performed throughout development on major organs where *H19* and
121 *Igf2* are highly expressed. In contrast to the liver where the paternal *hIC1* did not lead to significant
122 abnormal morphology (data not shown), severe developmental defects were found in the *+/hIC1* heart
123 and placenta. Cardiac defects in *+/hIC1* embryos were observed as early as E12.5, where the superior and
124 inferior endocardial cushions failed to fuse into a common AV cushion (Figure 2C). The cushion defect
125 preceded incomplete interventricular septum (IVS) formation. At E15.5, a severe perimembranous
126 ventricular septal defect (VSD) was observed in all 5 *+/hIC1* hearts that were evaluated (Figure 2C.

127 Importantly, this congenital heart defect resembles malformations reported in several SRS patients with
128 IC1 hypomethylation (Ghanim et al., 2013), although the prevalence is unclear and may reflect the degree
129 of mosaicism in SRS. Additionally, E15.5 hearts showed an extremely thin myocardium (Figure 2C).
130 Both VSD and thinned ventricular walls persisted in E17.5 *+/hIC1* hearts (Figure 2B, C). Additionally, 6
131 out of 16 *+/hIC1* hearts in the late gestation group (E15.5 to P0) had bicuspid pulmonary valve (BPV), a
132 rare cardiac defect in which the pulmonary valve only develops two cusps as opposed to the normal
133 tricuspid structure (Figure 2D and Supplemental Figure 1A). These results demonstrate that paternal *hIC1*
134 transmission results in variably penetrant cardiac phenotypes. Notably, atrioventricular valvuloseptal
135 morphogenesis, the fusion of the AV cushion and nascent septa during cardiogenesis, is required for
136 proper cardiac septation (Eisenberg & Markwald, 1995). Segmentation of the heart into four separate
137 chambers is required to establish distinct pulmonary and systemic blood flow during heart development
138 and is required to prevent the mixing of oxygenated and deoxygenated blood. We speculate that the
139 failure of *hIC1* mutants to establish complete ventricular septation could have led to a reduced ability to
140 provide oxygen and nutrient rich blood to the rest of the developing body (Savolainen, Foley, & Elmore,
141 2009; Spicer, Hsu, Co-Vu, Anderson, & Fricker, 2014).

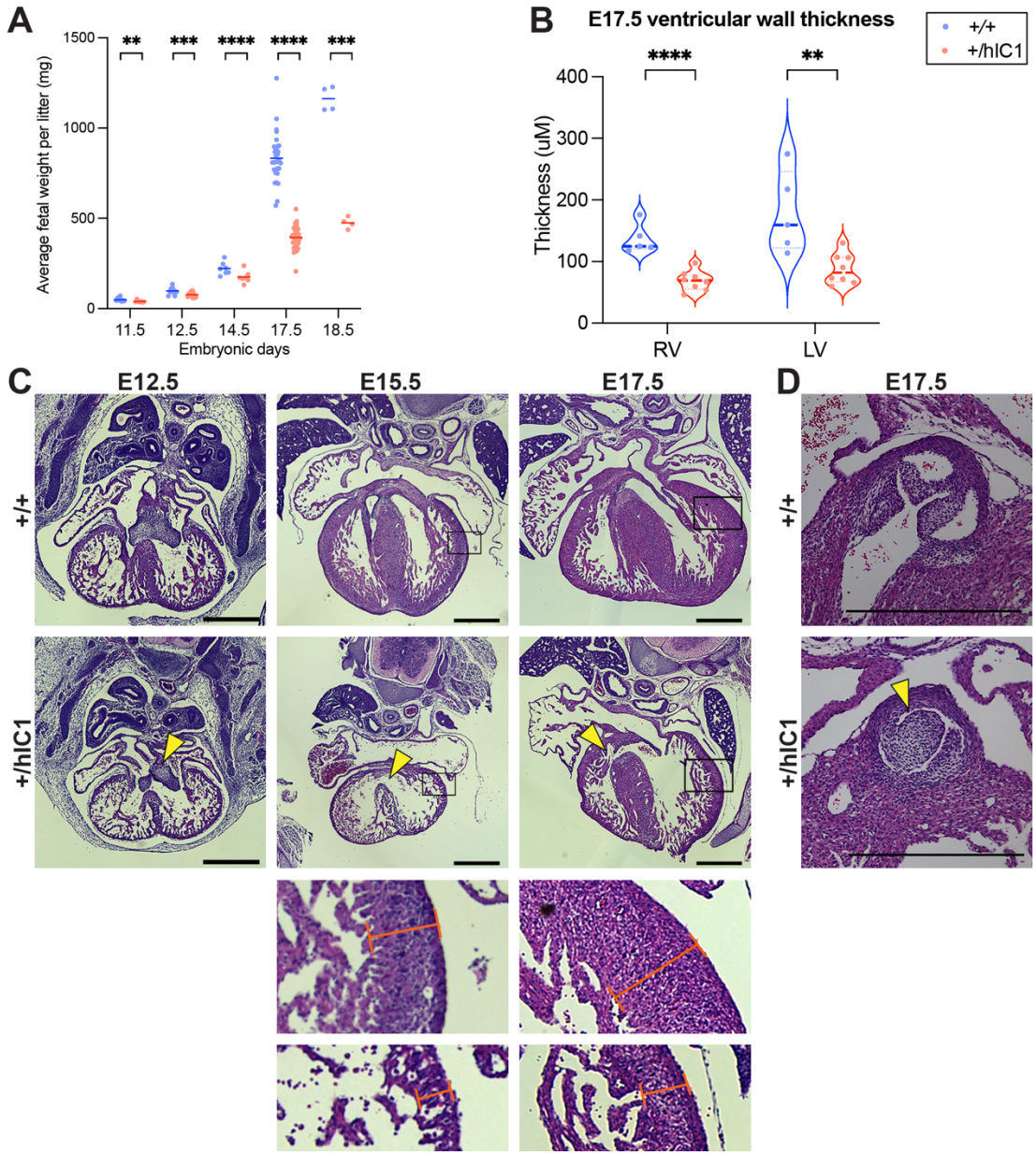

142

Figure 2. Growth anomalies and cardiac defects of *+/hIC1* embryos.

(A) Fetal weight of the wild-type (blue) and *+/hIC1* (red) embryos at E11.5, E12.5, E14.5, E17.5 and E18.5. Each data point represents an average weight of each genotype from one litter. 8 litters for E11.5, 10 litters for E12.5, 7 litters for E14.5, 31 litters for E17.5, 4 litters for E18.5 are presented. (B) Quantification of ventricular wall thickness (μm), measured from E17.5 wild-type and *+/hIC1* hearts. Each data point represents an individual conceptus. 5 wild-type and 8 *+/hIC1* embryos from four different litters were examined. (C) Representative cross-sections of wild-type and *+/hIC1* embryonic hearts at E12.5, E15.5 and E17.5, stained with hematoxylin and eosin. Note the lack of fusion between AV cushions at E12.5, the VSD at E15.5 and E17.5 in *+/hIC1* hearts (yellow arrowheads).

The boxed regions of E15.5 and E17.5 images are enlarged at the bottom of the figure, to show where the ventricular wall thickness is measured. Scale bars = 500 μm. (D) A representative image of pulmonary valves in E17.5 wild-type and *+/hIC1* hearts. The *+/hIC1* right pulmonary cusp is enlarged (yellow arrowhead) and there is no cusp in the anterior position, in contrast to the tricuspid structure in the wild-type heart. Scale bars = 500 μm. Statistics used are (A) multiple paired t-test and (B) multiple unpaired t-test with $^{**}P < 0.01$, $^{***}P < 0.001$, $^{****}P < 0.0001$ and ns = not significant.

Another major organ with high *H19/Igf2* expression, which forms early in development, is the placenta. Multiple developmental defects were observed in *+/hIC1* placentas. As previously described (Hur et al., 2016), *+/hIC1* placentas were growth restricted throughout development (Figure 3A), although the fetal to placental weight ratio was not affected through E15.5 (Supplemental Figure 2A). However, at E17.5, the fetal to placental weight ratio was lower in *+/hIC1* conceptuses, indicating that the fetal growth restriction was more severe than the placental growth restriction as the concepti neared term (Figure 3B). In addition to placental undergrowth, the junctional to labyrinth zone ratio was increased in *+/hIC1* placentas (Figure 3C), suggesting that the growth of the labyrinth layer, where the maternal-fetal exchange occurs, was more affected. Moreover, *H19* overexpression was exaggerated in the labyrinth in E17.5 *+/hIC1* placentas, while the *Igf2* depletion was consistent throughout the whole placenta (Figure 3D), indicating that *H19* overexpression contributed disproportionately to the phenotype of growth restriction in the labyrinth. Large thrombi were observed in the labyrinth zone of these *+/hIC1* placentas (Figure 3F), in a male-skewed manner (Figure 3E). As the thrombi could be formed due to defective vasculature structures, wild-type and *+/hIC1* placentas were stained for CD34, a marker for the fetoplacental endothelial cells that line the microvessels in the labyrinth layer (Figure 3G). Vessels in the *+/hIC1* labyrinth were highly dilated and had decreased density, which was confirmed by quantifying the stained areas on the images (Figure 3H and Supplemental Figure 2B). The reduced labyrinth layer and defective microvascular expansion likely compromised the ability of *+/hIC1* placentas to supply nutrients and oxygen to the fetus. These results support the hypothesis that the abnormal growth of *+/hIC1*

163 embryos may be explained by failure in multiple organs, especially the heart and placenta, which are

164 developmentally linked (Barak, Hemberger, & Sucov, 2019).

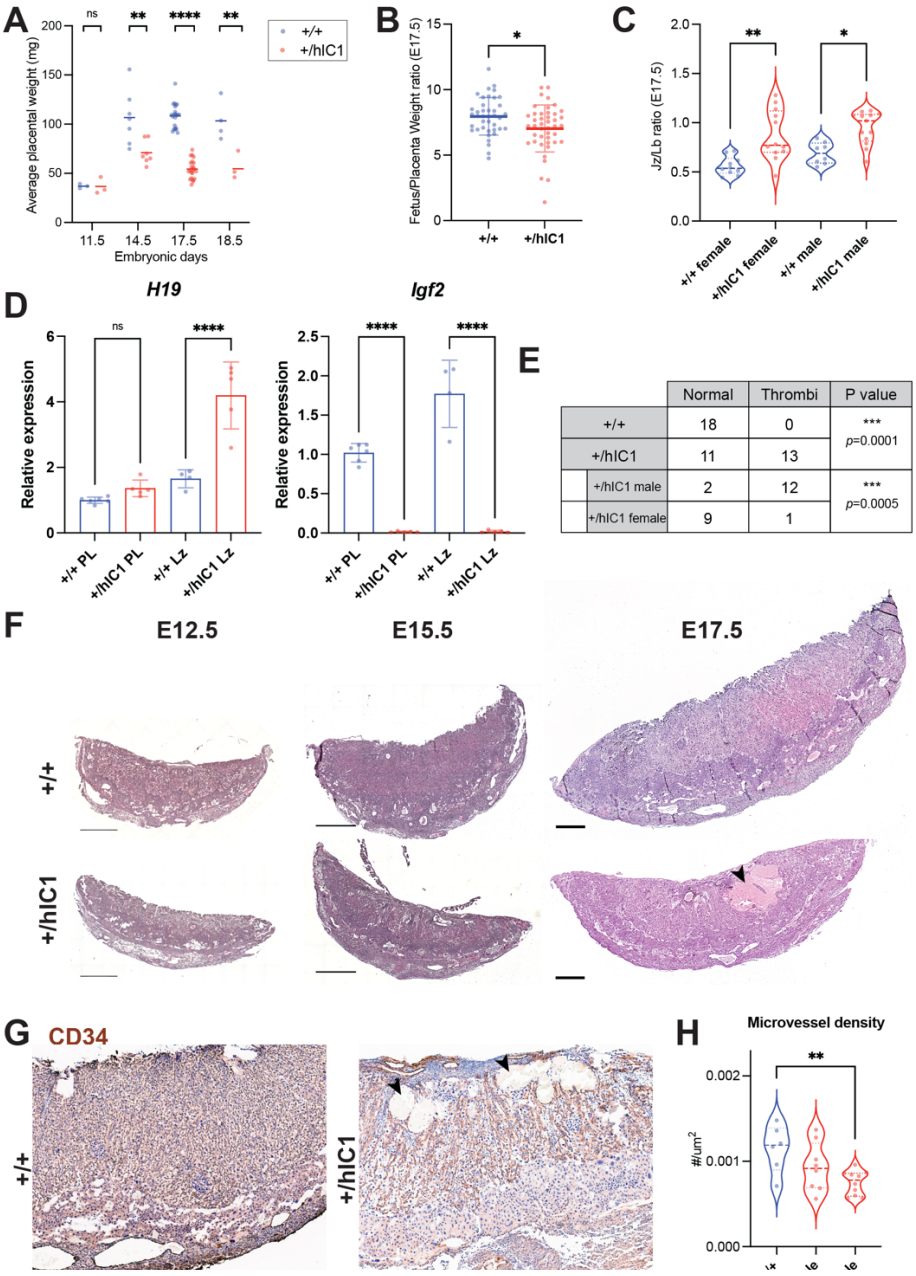

	Normal	Thrombi	P value
+/+	18	0	*** p=0.0001
+/hIC1	11	13	
+/hIC1 male	2	12	*** p=0.0005
+/hIC1 female	9	1	

165

Figure 3. Placental defects of *+/hIC1* embryos.

(A) Placental weight of the wild-type (blue) and *+/hIC1* (red) samples at E11.5, E14.5, E17.5 and E18.5. Each data point represents an average weight of each genotype from one litter. 3 litters for E11.5, 6 litters for E12.5, 7 litters for E14.5, 22 litters for E17.5, 4 litters for E18.5 are presented. (B) Fetal to placental weight ratios in E17.5 wild-type and *+/hIC1* samples (mean ± SD). 40 wild-type and

43 *+/hIC1* embryos from 22 litters are presented. (C) Junctional zone (Jz) to labyrinth (Lb) ratio in E17.5 wild-type and *+/hIC1* placentas. (D) Relative total expression of *H19* and *Igf2* in E17.5 wild-type and *+/hIC1* placentas and labyrinths (mean ± SD). (E) Number of wild-type, male and female *+/hIC1* placentas with thrombi observed. (F) Representative cross-sections of E12.5, E15.5 and E17.5 wild-type and *+/hIC1* placentas stained with hematoxylin and eosin. Black arrowhead indicates a large thrombus formed in the *+/hIC1* labyrinth. Scale bars = 1mm. (G) Representative images of CD34 immunostaining counterstained with hematoxylin on E17.5 wild-type and *+/hIC1* placental sections. Black arrowheads indicate thrombi in the *+/hIC1* labyrinth. Scale bars = 1mm. (H) Quantification of the microvessel density in E17.5 wild-type and *+/hIC1* placentas. 11 wild-type, 12 *+/hIC1* male, 10 *+/hIC1* female placentas from 8 litters were quantified. (B, C, D, H) Each data point represents an individual conceptus from different litters. Statistics used are (A) multiple paired t-test, (B) unpaired Student's t-test, (C, D, H) one-way ANOVA with Tukey's multiple comparisons test, (E) Fisher's exact test. *$P < 0.05$, **$P < 0.01$, ***$P < 0.001$, ****$P < 0.0001$, ns = not significant.

Normalizing *H19* expression partially rescues paternal *hIC1* defects

It has been previously reported that *Igf2* null mice are viable (DeChiara et al., 1991). Thus, we hypothesize that *H19* overexpression combined with a loss of *Igf2* expression is the molecular contributor to the lethality of paternal *hIC1* transmission. To examine if reduced *H19* expression would rescue the paternal *hIC1* transmission phenotypes, we generated a mouse model with deletion of the *H19* transcription unit [$H19^{\Delta 2.8kb\text{-}H19}$; shortened as *ΔH19*] (Figure 1B, Supplemental Figure 3A and B). Consistent with previous reports, maternal deletion of *H19* [*ΔH19/+*] led to an absence of *H19* expression and tissue-specific minimal activation of maternal *Igf2* (Supplemental Figure 3C). These mice are viable and fertile, regardless of whether the deletion is maternally or paternally transmitted, although maternal transmission is associated with increased fetal weight from E14.5 and onwards (Supplemental Figure 3D and data not shown).

Heterozygous *ΔH19* females were mated with heterozygous *hIC1* males to generate *ΔH19/hIC1* embryos. These embryos were expected to have lower *H19* expression compared to *+/hIC1* embryos, as the maternal *H19* expression was silenced (Figure 4A). Among four possible genotypes from this breeding, *+/hIC1* embryos constituted approximately 15% per litter at E17.5, as opposed to the expected Mendelian ratio of 25%. In contrast, *ΔH19/hIC1* embryos comprised approximately 30% per litter at

183 E17.5, indicating partial rescue of the resorption frequency by maternal *H19* deletion (Figure 4B and
184 Supplemental Figure 4A). However, *ΔH19/hIC1* embryos still exhibited perinatal lethality, with no live
185 pups observed on the day of birth. With respect to growth restriction, the maternal *ΔH19* allele partially
186 rescued the phenotype. At E11.5, *ΔH19/hIC1* fetal weight was not significantly different from wild-type
187 littermates (Figure 4C). However, at late gestation (E17.5), although *ΔH19/hIC1* fetuses had a significant
188 increase in fetal weight compared to the *+/hIC1* fetuses, *ΔH19/hIC1* fetuses remained significantly
189 smaller compared to wild-type. As perinatal lethality was still observed, conceptuses were analyzed
190 histologically to characterize their developmental defects. The AV cushion defect persisted in all
191 examined E13.5 *ΔH19/hIC1* embryos, and 50% of the examined E17.5 *ΔH19/hIC1* hearts showed either
192 perimembranous or muscular VSDs (Figure 4D). Thrombi were still present in approximately 50% of
193 *ΔH19/hIC1* placentas (Figure 4E), and placental weight remained significantly lower compared to wild-
194 type littermates (Supplemental Figure 4B). Of note, none of these histological defects were observed in
195 *ΔH19/+* embryonic hearts and placentas (Figure 4D and data not shown; 3 *ΔH19/+* hearts each from
196 E13.5, E15.5 and E17.5 concepti, and 20 E17.5 *ΔH19/+* placentas were examined). E17.5 *ΔH19/hIC1*
197 tissues demonstrated wild-type levels of *H19* expression, while the *Igf2* expression remained markedly
198 lower than wild-type (Figure 4F and Supplemental Figure 4C). From these results, we conclude that
199 restoring *H19* expression is not sufficient to rescue completely the lethality and developmental defects
200 upon paternal transmission of *hIC1*. Thus, phenotypes are likely caused by abnormal expression of both
201 *H19* and *Igf2*.

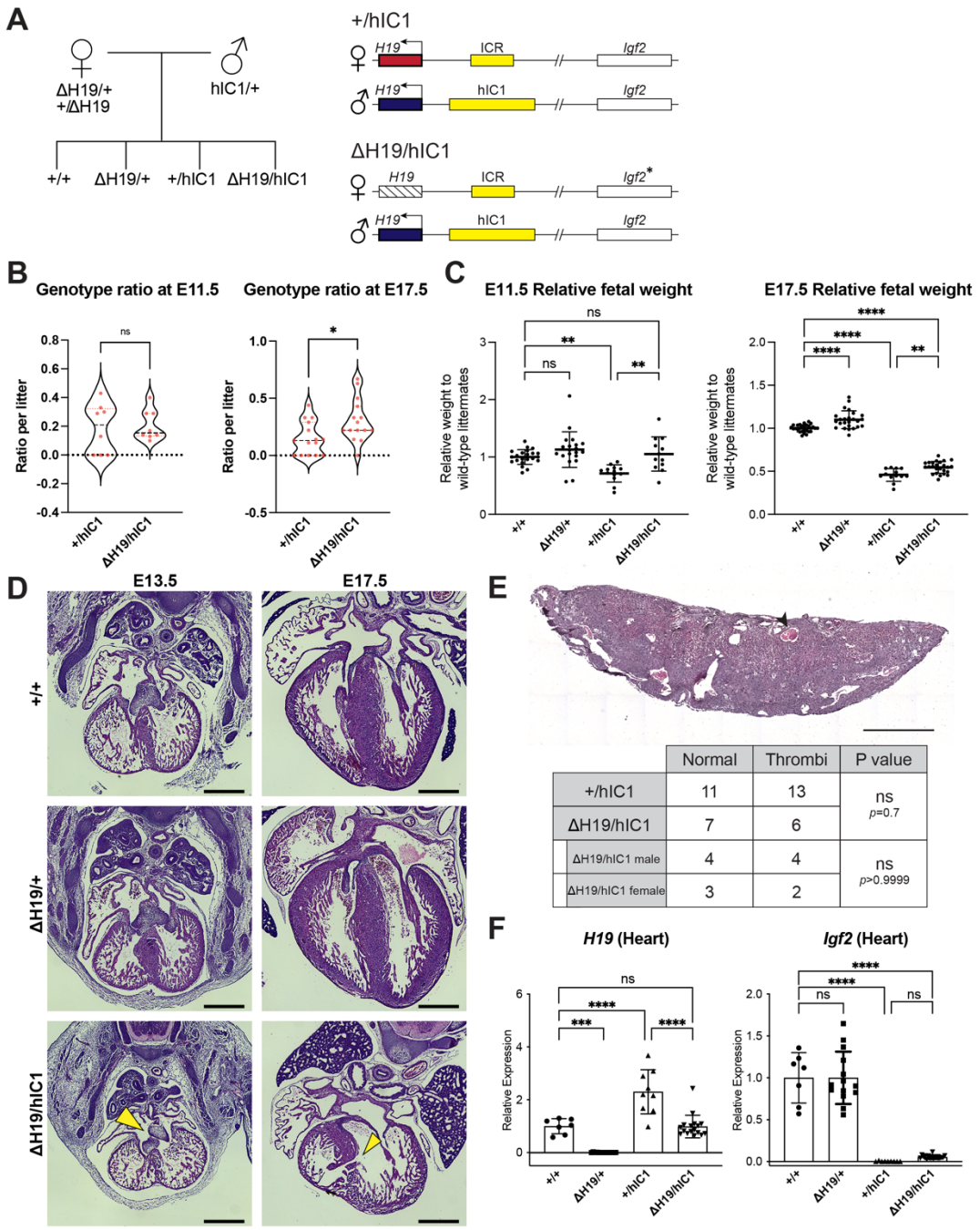

202

Figure 4. Normalizing *H19* expression through the maternal deletion of *H19*.

(A) A schematic representation of the rescue breeding between *ΔH19* heterozygous female and *hIC1/+* male mice is depicted. *ΔH19/hIC1* embryos are expected to express *H19* only from the paternal allele, and maternally express *Igf2* in a tissue-specific manner. (B) Ratio of *+/hIC1* and *ΔH19/hIC1* embryos observed in E11.5 and E17.5 litters (8 E11.5 litters and 15 E17.5 litters with litter size larger than 5 pups were examined). Each data point represents one litter. (C) Relative fetal weights of wild-type, *ΔH19/+, +/hIC1* and *ΔH19/hIC1* embryos at E11.5 and E17.5, normalized to the

average body weight of the wild-type littermates (mean ± SD). (D) Representative cross-sections of wild-type, *⊿H19/+* and *⊿H19/hIC1* embryonic hearts at E13.5 and E17.5, stained with hematoxylin and eosin. Note the cushion defect at E13.5 and the VSD at E17.5 in *⊿H19/hIC1* hearts (yellow arrows). Scale bars = 500 μm. (E) (Top) Representative cross-section of E17.5 *⊿H19/hIC1* placenta stained with hematoxylin and eosin. Black arrowhead indicates a thrombus. Scale bar = 1mm. (Bottom) Number of the wild-type, male and female *+/hIC1* placentas with thrombi observed. (F) Relative total expression of *H19* and *Igf2* in E17.5 wild-type, *⊿H19/+, +/hIC1* and *⊿H19/hIC1* hearts (mean ± SD). (C, F) Each data point represents an individual conceptus from different litters. Statistics used are (B, C, F) one-way ANOVA with Tukey's multiple comparisons test and (E) Fisher's exact test. **P* < 0.05, ***P* < 0.01, ****P* < 0.001, *****P* < 0.0001, ns = not significant.

Paternal *hIC1* defects are rescued by deletion of the maternal *H19/Igf2* ICR

Finally, we utilized a previously published mouse model with a 3.8-kb deletion spanning the *H19/Igf2* ICR [$H19^{\Delta 3.8kb\text{-}5'H19}$; shortened as *⊿3.8*] to modulate both *H19* and *Igf2* expression (Thorvaldsen et al., 2006, 2002). Absence of the maternal *H19/Igf2* ICR activates the maternal *Igf2* allele and reduces *H19* expression. Thus, *Igf2* expression from the maternal allele in *⊿3.8/hIC1* embryos was expected to restore *Igf2* levels (Figure 5A).

Crosses between heterozygous *⊿3.8* females and heterozygous *hIC1* males produced the expected Mendelian ratio of offspring with *⊿3.8/hIC1* mice appearing fully viable. Both fetal and placental weights were not significantly different between *⊿3.8/hIC1* and wild-type concepti at E17.5 (Figure 5B and Supplemental Figure 5A), demonstrating full rescue of the lethality and growth restriction. However, a subset of *⊿3.8/+* and *⊿3.8/hIC1* embryonic hearts (3 out of 6 *⊿3.8/+* hearts and 2 out of 5 *⊿3.8/hIC1* hearts) had VSDs, although the lesions in the IVS were smaller than those found in *+/hIC1* hearts (Figure 5C). While *Igf2* expression in the E17.5 *⊿3.8/hIC1* hearts was restored to wild-type levels, normalization of *H19* expression varied among embryos. Although not statistically significant in heart, *⊿3.8/hIC1* embryos tended to have higher *H19* expression compared to the wild-type littermates (Figure 5D and Supplemental Figure 5B). These results suggest that the physiological levels of *H19* and *Igf2* expression are critical for normal cardiac development, and the variability in *H19* rescue could help to explain the

221 varying penetrance of the cardiac phenotype. No thrombi were detected in the *Δ3.8/hIC1* placentas, and
222 the placental morphology was normal with the junctional to labyrinth zone ratio not significantly different
223 compared to wild-type (Supplemental Figure 5C). In sum, restoring both *H19* and *Igf2* to near wild-type
224 levels was necessary for the full rescue of the most severe pathologies of paternal *hIC1* transmission.

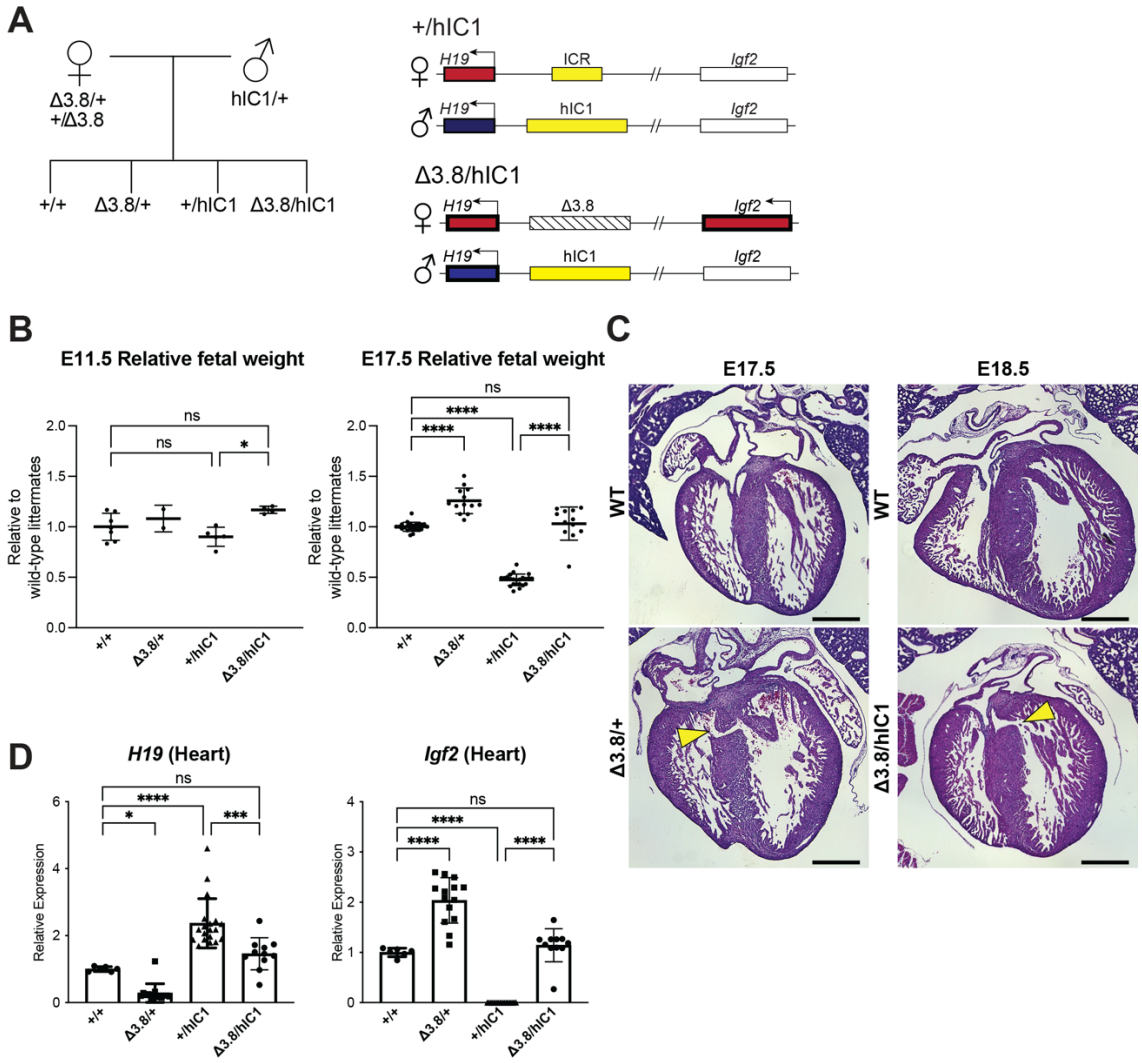

225

226

Figure 5. Restoring *H19* and *Igf2* expression utilizing maternal *H19/Igf2* ICR deletion.
(A) A schematic representation of the offspring produced when *Δ3.8* heterozygous female and *hIC1/+* male mice are mated is depicted. *Δ3.8/hIC1* embryos are expected to show activation of maternal *Igf2* expression as well as paternal *H19* expression. (B) Relative fetal weights of wild-type, *Δ3.8/+, +/hIC1,* and *Δ3.8/hIC1* embryos at E11.5 and E17.5, normalized to the average body weight of wild-type littermates (mean ± SD). 2 E11.5 and 10 E17.5 litters are presented. (C) Representative cross-sections of E17.5 *Δ3.8/+* and E18.5 *Δ3.8/hIC1* embryonic hearts with VSDs (yellow arrows), stained

with hematoxylin and eosin. Sections from wild-type littermates are shown together for comparison. Scale bars = 500 μm. (D) Relative total expression of *H19* and *Igf2* in E17.5 wild-type, *⊿3.8/+, +/hIC1,* and *⊿3.8/hIC1* hearts (mean ± SD). (B, D) Each data point represents an individual conceptus from different litters. One-way ANOVA with Tukey's multiple comparisons test was used with *$P < 0.05$, ***$P < 0.001$, ****$P < 0.0001$ and ns = not significant.

227

228 **Transcriptomic analysis of cardiac endothelial cells with various *H19/Igf2* expression**

229 Severe cardiac phenotypes associated with paternal *hIC1* transmission prompted us to question
230 the mechanism of how dysregulated *H19/Igf2* causes such developmental defects. The paternal *hIC1*-
231 associated cardiac phenotypes were observed as early as E12.5 when AV cushion fusion is delayed in
232 developing hearts (Figure 2B), making E12.5 an optimal time point to identify the key pathways of valve
233 development and cardiac septation that are disrupted by *H19/Igf2* dysregulation. Endothelial and
234 endothelial-derived cells comprise the majority population in the AV cushion and majority non-myocyte
235 population of the ventricular septum at E12.5 (Von Gise & Pu, 2012). Moreover, both *H19* and *Igf2* are
236 strongly expressed in the endocardial layer of developing heart (García-Padilla, Domínguez, Aránega, &
237 Franco, 2019). Therefore, transcriptomic analysis was performed on cardiac endothelial cells of each
238 mutant.

239 CD31+ cardiac endothelial cells from E12.5 wild-type, *+/hIC1*, *⊿H19/+, ⊿H19/hIC1*, *⊿3.8/+,*
240 and *⊿3.8/hIC1* embryos were collected for RNA sequencing. First, we confirmed that these 6 groups
241 show gradual alteration of *H19*/*Igf2* expression (Figure 6A), which enabled us to generate multiple
242 comparisons relative to *H19* and *Igf2* levels and potentially enabling attribution of phenotypes to *H19* or
243 *Igf2*. Notably, *H19*/*Igf2* expression was indistinguishable in the wild-type and *⊿3.8/hIC1* samples.
244 Additionally, there were no sex-specific differences in *H19*/*Igf2* expression across all the groups.

245 To elucidate candidate genes and cellular processes in conferring the paternal *hIC1*-specific
246 cardiac phenotypes, we compared *+/hIC1* and wild-type samples. This comparison resulted in 224
247 significant differentially expressed genes (DEGs) (Figure 6B, left). Gene ontology (GO) analysis revealed

248 that pathways related to proliferation and remodeling of endothelial and epithelial cells are enriched in
249 these DEGs (Figure 6B, right) (Mi, Muruganujan, Ebert, Huang, & Thomas, 2019). Notably, genes
250 involved in extracellular matrix (ECM) and specifically, collagen matrix production, were differentially
251 enriched in E12.5 *+/hIC1* samples; consistent with increased collagen in the E17.5 *+/hIC1* hearts, as
252 confirmed through immunofluorescence staining (Figure 6C, Supplemental Figure 6A and B). Thus,
253 differential gene expression in the presence of paternal *hIC1* was evidenced by E12.5 and correlated with
254 histological consequences persisting through gestation.

255 Because cardiac phenotypes were indistinguishable between males and females, we next used
256 same-sex comparisons between *+/hIC1* and wild-type to identify the *hIC1*-specific DEGs that are
257 significant in both males and females (Figure 6D, left and Supplemental Figure 6C). The 25 genes that
258 overlapped between male and female *+/hIC1*-specific DEGs included *Col14a1,* which was upregulated in
259 *+/hIC1*, emphasizing the importance of collagen-related ECM in *hIC1*-associated cardiac defects. The
260 expression pattern of these 25 genes across all samples clustered *+/hIC1* and *ΔH19/hIC1*, the two groups
261 with the most severe cardiac defects and perinatal lethality (Figure 6D, right).

262 To separate the effect of *Igf2* depletion from that of *H19* overexpression, we utilized *ΔH19/hIC1*
263 samples. Consistent with previous observations from E17.5 hearts (Figure 4F), *ΔH19/hIC1* endothelial
264 cells exhibited low *Igf2,* but *H19* expression was not significantly different from wild-type (Supplemental
265 Figure 7A). Thus, *ΔH19/hIC1* samples were compared to *+/hIC1* to clarify the sole effect of *H19*
266 overexpression. Here, 46 DEGs were identified (Supplemental Figure 7B), which were enriched in
267 vascular endothelial cell proliferation pathways (Supplemental Figure 7C). Surprisingly, although
268 physiologically similar to *+/hIC1,* the *ΔH19/hIC1* transcriptome was quite different from that of *+/hIC1.*
269 Compared to wild-type, *ΔH19/hIC1* only had 23 DEGs (Supplemental Figure 7A), in contrast to *+/hIC1*
270 showing more than 200 DEGs compared to wild-type (Figure 6B, left). This result underscores the
271 overwhelming effect of increased *H19* in transcriptomic regulation.

272 We then analyzed *Δ3.8/hIC1* samples to identify cellular processes that are required to rescue the
273 paternal *hIC1*-associated lethality, as *Δ3.8/hIC1* mice are fully viable with occasionally observed VSD.
274 While *Δ3.8/hIC1* had only two DEGs compared to wild-type (Figure 6E), 487 genes were differentially
275 expressed in *Δ3.8/hIC1* compared to *+/hIC1* (Supplemental Figure 8A). Within these DEGs, we wanted
276 to clarify the genes that were likely involved in restoring viability. The 487 DEGs between *+/hIC1* and
277 *Δ3.8/hIC1* were compared to the DEGs between *+/hIC1* and wild-type to filter genes that are commonly
278 affected in both comparisons (Figure 6F, left). GO analysis showed that the 116 overlapping genes are
279 associated with endothelial/epithelial cell proliferation and remodeling (Supplemental Figure 8B),
280 emphasizing the importance of the proper regulation of these pathways in the rescued viability of
281 *Δ3.8/hIC1* embryos. The expression pattern of these 116 genes clustered *+/hIC1* and *ΔH19/hIC1*,
282 implicating these genes in the perinatal lethality characteristic of these two groups (Figure 6F, right).

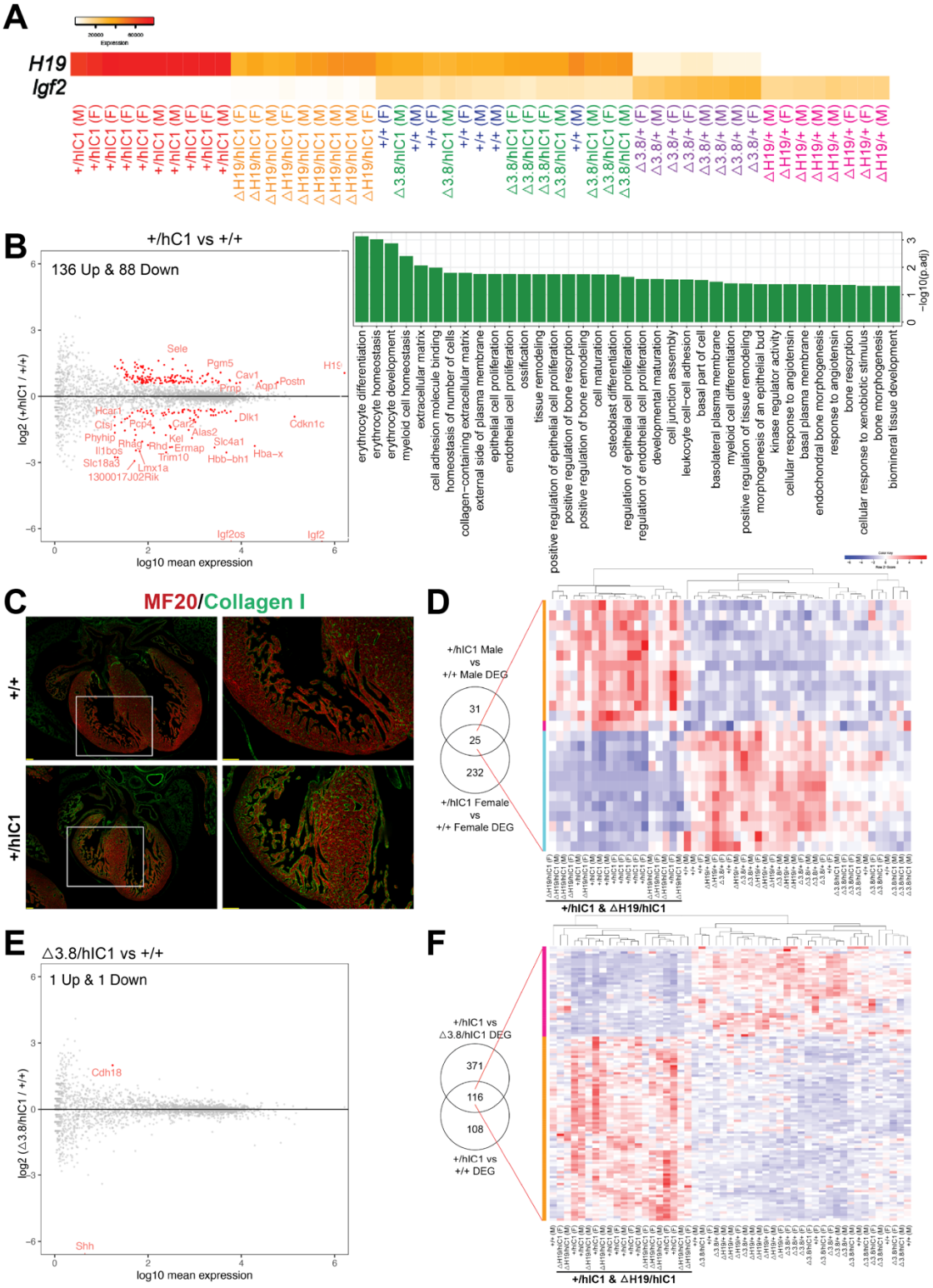

Figure 6. Transcriptomic analysis of E12.5 cardiac endothelial cells from wild-type and mutant embryos.

(A) A gradient *H19* and *Igf2* expression levels are depicted in E12.5 wild-type, *+/hIC1, ⊿H19/+, ⊿H19/hIC1, ⊿3.8/+* and *⊿3.8/hIC1* cardiac endothelial cells. M: Male, F: Female. (B) (Left) Comparison between *+/hIC1* and the wild-type samples with a volcano plot shows 224 DEGs between *+/hIC1* and the wild-type samples. (Right) GO pathways that are enriched for the 224 DEGs. (C) Immunofluorescence staining for MF20 (red) and collagen (green) on E17.5 wild-type and *+/hIC1* hearts. Images on the right are enlarged from the boxed area of images on the left. Scale bars = 100 μm. (D) Expression pattern of 25 genes that are differentially expressed in both male and female *+/hIC1* samples is compared to wild-type. (E) A volcano plot represents 2 DEGs between *⊿3.8/hIC1* and the wild-type samples. (F) Expression pattern of 116 genes that are commonly differentially expressed in *+/hIC1* compared to the wild-type and *⊿3.8/hIC1* samples.

Discussion

In this study, we report that the overexpression of *H19* combined with *Igf2* depletion leads to severe morphological defects in the heart and placenta, which are likely to be involved with the perinatal lethality and restricted growth of SRS mouse models. Genetically correcting *H19* was not sufficient to fully rescue the developmental defects, indicating that the SRS-like phenotypes of paternal *hIC1* transmission are not solely attributable to *H19* overexpression. Unexpectedly, although moderately adjusting both *H19* and *Igf2* rescued the lethality, septal defects persisted in some of the *⊿3.8/hIC1* embryos, suggesting that cardiac development is extremely sensitive to the dosage of *H19* and *Igf2.* Our transcriptomic profiling of cardiac endothelial cells with various levels of *H19* and *Igf2* expression uncovers critical pathways driven by *H19* and *Igf2* that are important for cardiac structure formation. The result suggests that the regulation of ECM and proliferation of endothelial cells are tightly regulated by *H19* and *Igf2,* and potentially responsible for the paternal *hIC1*-associated cardiac defects.

The function of *H19* in cardiac development is understudied even though the expression of *H19* is robust in the developing endocardium and epicardium throughout gestation (García-Padilla et al., 2019). Abnormal *H19/Igf2* expression in *+/hIC1* hearts disrupted AV cushion fusion, ventricular septation and valve formation processes with variable penetrance. These events require properly established ECM, which accommodates endothelial-mesenchymal transition, cell proliferation, and cell-cell adhesion in

303 developing hearts (Kruithof, Krawitz, & Gaussin, 2007; Sullivan & Black, 2013; Von Gise & Pu, 2012).
304 In adult murine hearts, where *H19* has been well implicated in cardiac fibrosis and remodeling (Greco et
305 al., 2016; Hobuß et al., 2020; Lee et al., 2011; Wang, Sun, & Sun, 2021), *H19* overexpression led to
306 increased ECM and fibrosis markers after myocardial injury, while deleting *H19* resulted in
307 downregulated ECM genes (Choong et al., 2019). In our *+/hIC1* endothelial cells, the expression of
308 several key ECM genes such as *Periostin* (*Postn*) (Snider, 2009; Sullivan, 2013), *Col14a1*, and *Adamts17*
309 (Hubmacher, 2015) was significantly upregulated compared to wild-type cells. Combined with increased
310 collagen in E17.5 *+/hIC1* hearts (Figure 6C), we hypothesize that failing to establish proper ECM
311 contributes significantly to the *+/hIC1*-associated cardiac defects during development. Additionally,
312 regulators of cell proliferation, including *E2f5, Trabd2b,* and *Septin4,* and genes associated with
313 inflammation such as *Sele* and *Cd200* were also differentially expressed in *+/hIC1* samples. Overall, this
314 work provides some hints regarding the potential mechanism underlying how increased *H19* expression
315 disrupts normal cardiac development.

316 To identify the genes whose expression is solely affected by *H19,* we compared *+/hIC1,*
317 *ΔH19/hIC1,* and *ΔH19/+* endothelial cells. Among 224 genes that are differentially expressed in *+/hIC1*
318 endothelial cells relative to wild-type, 15 genes are also differentially expressed in *ΔH19/hIC1* samples,
319 suggesting that these 15 genes were affected by the loss of *Igf2* rather than increased *H19.* Among the
320 remaining 209 DEGs that are not altered in *ΔH19/hIC1* samples, only *Fgf10* and *H19* were also
321 differentially expressed in *ΔH19/+* endothelial cells compared to wild-type. *Fgf10,* a key regulator of
322 cardiac fibroblast development, mediates communication between cardiac progenitor cells and regulates
323 cardiac myocyte proliferation (Hubert, Payan, & Rochais, 2018; Vega-Hernández, Kovacs, de Langhe, &
324 Ornitz, 2011). Consistently, *Fgf10* null mouse embryos showed abnormal cardiac morphology with
325 reduced heart size and thinned ventricular wall (Rochais et al., 2014; Vega-Hernández et al., 2011). In our
326 samples, *Fgf10* is upregulated when *H19* is deleted and downregulated upon *H19* overexpression, linking
327 *H19* and *Fgf10* closely in the context of cardiac development. Additionally, Gene Set Enrichment
328 Analysis (GSEA) revealed that the set of imprinted genes (BRIDEAU_IMPRINTED_GENES) including

329 *Cdkn1c, Dlk1* and *Gatm* was differentially enriched in *+/hIC1* samples (Supplemental Figure 9A)
330 (Mootha et al., 2003; Subramanian et al., 2005). The same set of genes was also differentially enriched in
331 *ΔH19/+* samples (Supplemental Figure 9B), but not *ΔH19/hIC1* (Supplemental Figure 9C), underscoring
332 a role for *H19* as a master regulator of the imprinted gene network (IGN) (Gabory, Jammes, & Dandolo,
333 2010).

334 In contrast to the less well understood role for *H19*, *Igf2* is the main growth factor in the
335 developing ventricular wall. Similar to *H19, Igf2* is highly expressed in the developing cardiac
336 endocardium and epicardium from early gestation (Shen et al., 2015) before ventricular septation is
337 completed (Savolainen et al., 2009). Deletion of *Igf2* and its receptors caused decreased cardiomyocyte
338 proliferation and ventricular hypoplasia, suggesting that *Igf2* is the major regulator of ventricular wall
339 thickening (Li et al., 2011; Shen et al., 2015). Additionally, the interventricular septum is comprised of
340 both mesenchymal and muscular components (Penny & Vick, 2011; Spicer et al., 2014), and a reduction
341 in cardiomyocyte proliferation can lead to VSD (Snider & Conway, 2011). Thus, the lack of *Igf2,* a
342 growth promoter for cardiomyocytes, could have contributed to the septal defects observed in *+/hIC1* and
343 *ΔH19/hIC1* hearts. However, the thinned myocardium in *Igf2* knockout mouse embryos was resolved by
344 birth, resulting in normal cardiac morphology in neonates (Shen et al., 2020). In contrast, ventricular wall
345 thinning and septal defects in *+/hIC1* and *ΔH19/hIC1* hearts were aggravated towards the end of
346 gestation, indicating that these phenotypes are not exclusively attributable to the loss of *Igf2* expression.

347 Recovery of *Igf2* expression in *Δ3.8/hIC1* hearts rescued ventricular hypoplasia, consistent with
348 previous findings (Li et al., 2011; Shen et al., 2015). In contrast, septal defects persist in some *Δ3.8/+* and
349 *Δ3.8/hIC1* embryos. Because *Igf2* expression varied substantially among *Δ3.8/+* and *Δ3.8/hIC1* hearts
350 (Figure 5D), we hypothesize that the varying penetrance of septal defects in these hearts reflects the range
351 of *H19/Igf2* levels. The only upregulated gene in *Δ3.8/hIC1* endothelial cells compared to wild-type was
352 *Cadherin 18 (Cdh18)* (Figure 6E), which was also upregulated in *Δ3.8/+* samples compared to wild-type
353 (Supplemental Figure 8C) and clinically reported to be mutated in CHDs including VSD (Chen et al.,

354 2018; Soemedi et al., 2012). Although we and others showed that restoring *Igf2* successfully rescues the
355 growth restriction in SRS-like mouse models (Han, Szabó, & Mann, 2010; Liao et al., 2021), septal
356 defects caused by *H19* and *Igf2* dysregulation are reported for the first time in this study. Our data provide
357 evidence that ventricular septation may be regulated separately from the ventricular wall thickening, and
358 that both events are extremely sensitive to the level of *H19* and *Igf2* expression. In humans, VSDs were
359 found in SRS patients with IC1 hypomethylation (Ghanim et al., 2013) and a patient carrying
360 chromosomal gain of chr11p15 (Serra et al., 2012). Thus, the VSD observed in our mouse models nicely
361 models the SRS-associated CHD in human patients. It should be noted, however, that mice are often more
362 susceptible to VSDs than humans. Mice with VSDs show a higher neonatal mortality rate, possibly due to
363 the higher heart rates and relatively larger size of VSD lesions (Snider & Conway, 2011). Additionally,
364 cardiac defects that are lethal in mice can lead to spontaneous miscarriages in humans due to longer
365 human gestation, making it difficult to observe human infants with similar defects.

366 Linked through fetoplacental blood circulation, the heart and placenta are closely connected
367 under the cardiac-placental axis, which is crucial for fetal growth and viability (Barak et al., 2019;
368 Maslen, 2018). Both organs are responsible for supplying nutrients and oxygen for developing fetuses,
369 and placental and cardiac defects are often coupled in mouse models (Perez-Garcia et al., 2018) and
370 humans (Matthiesen et al., 2016; Rychik et al., 2018). Placental maintenance of a normoxic fetal
371 environment is vital for cardiac morphogenesis, and hypoxia can lead to severe defects emerging
372 especially in cushions and septa (Dor et al., 2001). Epicardial *Igf2* expression in developing ventricles is
373 induced by a normoxic environment that is dependent on the placental function (Shen et al., 2015), while
374 *H19* is upregulated under hypoxic conditions in mouse cardiomyocytes (Choong et al., 2019). This
375 suggests that *H19* and *Igf2* are important mediators of the interaction between heart and placenta.
376 Consistent with previous reports, gene sets of which expression is altered under hypoxic conditions
377 (HALLMARK_HYPOXIA, GROSS_HYPOXIA_VIA_HIF1A_DN) are differentially enriched in our
378 *+/hIC1* endothelial cells compared to wild-type (data not shown). As the heart and placenta are
379 responsible for meeting the fetal demand for nutrients and oxygen, the malfunction of these two organs

380 would severely constrain embryonic growth. Therefore, the precise role of *H19* and *Igf2* in cardiac-
381 placental communication needs to be clarified to understand how the SRS-related growth restriction is
382 induced by IC1 hypomethylation.

383 The labyrinth, where *+/hIC1* placentas show abnormal vasculature morphology and thrombosis,
384 serves as a prime location for maternal-fetal blood exchange (Woods, Perez-Garcia, & Hemberger, 2018).
385 Placental thrombosis can be caused by defective labyrinth integrity, and diminished labyrinth function
386 could limit the nutritional and oxygen supply for a fetus, which can, in turn, lead to hypoxia and growth
387 restriction. Both *H19* and *Igf2* are highly expressed in fetoplacental endothelial cells in the labyrinth
388 (Aykroyd, Tunster, & Sferruzzi-Perri, 2022; Sandovici et al., 2022). Genetically depleting *Igf2* expression
389 in epiblast lineage led to decreased labyrinth size and caused the formation of thrombi in the labyrinth,
390 although the lesions were smaller in size than those observed in *+/hIC1* placentas (Sandovici et al., 2022).
391 Depletion of the placental-specific *Igf2* transcript in mice resulted in smaller labyrinth and fetal growth
392 restriction (Constância et al., 2002; Sibley et al., 2004), although these mice showed an increased fetal to
393 placental weight ratio, which was decreased in *+/hIC1* mice. This contrasting result could be explained by
394 the effect of the increased *H19* expression in *+/hIC1* mice. *H19* regulates vascular endothelial growth
395 factor (VEGF) in human endothelial cells *in vitro* (Conigliaro et al., 2015), which is involved in placental
396 angiogenesis, specifically for the branching of fetoplacental vessels beginning at mid-gestation (Woods
397 et al., 2018). Additionally, *H19* is highly expressed in trophoblasts (Marsh & Blelloch, 2020; Poirier et
398 al., 1991), and disrupted trophoblast development leads to defective vascular branching in the labyrinth
399 and restricted fetal growth (Ueno et al., 2013). Thus, it is possible that the morphological anomalies
400 observed in the *+/hIC1* placenta are exaggerated by abnormal *H19* expression in trophoblasts.

401 In summary, we provide evidence that the proper dosage of *H19* and *Igf2* is essential for normal
402 cardiac and placental development. Investigation of the role of *H19* and *Igf2* in the cardiac-placental axis
403 will enable a better understanding of how paternal *hIC1* transmission leads to the SRS-like growth
404 restriction and perinatal lethality. As many patients with SRS exhibit DNA methylation mosaicism, the
405 distribution of the epimutation, which reflects the severity of patient symptoms, varies. This work

406 provides insight into identifying organs that are most sensitive to *H19* and *Igf2* dysregulation, which
407 would allow us to develop early intervention methods for critical SRS pathologies with such variabilities.
408

409 **Materials and Methods**

410 **Animal studies.** All studies were approved by the Institutional Animal Care and Use Committee
411 (IACUC) at the University of Pennsylvania. *hIC1* (Hur et al., 2016) and *Δ3.8* (Thorvaldsen et al., 2006,
412 2002) mouse models were previously described. Generation of *ΔH19* line is described in Supplemental
413 Information. Timed breeding was performed as previously described (SanMiguel, Abramowitz, &
414 Bartolomei, 2018). Vaginal sperm plugs were checked to calculate the age, and the day of the plug was
415 marked as E0.5. Visual staging confirmed the embryonic days at the time of dissection. All mice were
416 maintained on C57BL/6 background for more than 10 generations if not noted otherwise. Genotyping was
417 performed as described in Supplemental Information.

418 **Gene Expression Analysis.** Mouse tissues were ground using pestles, syringes and needles in either
419 TRIzol (Thermo Fisher scientific, Waltham, MA) or RLP buffer included in RNeasy Mini kit (Qiagen,
420 Hilden, Germany). RNA was isolated according to the manufacturer's instructions. cDNA synthesis,
421 qRT-PCR, and allele-specific expression analysis was performed as previously described (Hur et al.,
422 2016). Primers and PCR conditions are listed in Supplemental Table 1. RNA Sequencing library
423 preparation and analysis are described in Supplemental Information.

424 **Histological analysis.** Mouse heart and placenta samples were collected in cold PBS, fixed overnight in
425 4% paraformaldehyde or 10% phosphate-buffered formalin and processed through ethanol dehydration.
426 Tissues were paraffin-embedded and sectioned for further staining analysis. Hematoxylin and eosin
427 staining was performed using a standard protocol. Immunohistochemistry for MF20 (Developmental
428 Studies Hybridoma Bank, Iowa City, IA) and Collagen I (cat# ab34710, Abcam, Cambridge, UK) was
429 performed with primary antibody incubations overnight at 4°C. Prior to antibody incubation, antigen
430 retrieval with citrate buffer was performed, followed by a 1 hour block in 10% normal serum. DAPI
431 (cat#32670-5MG-F, Sigma-Aldrich, St. Louis, MO) was used as a counter stain, and slides were mounted

with VECTASHILD (Vector, Burlingame, CA). Images were taken on a Leica DMi8S widefield microscope. Placental CD34 staining was previously described (Vrooman et al., 2020). The thickness of ventricular wall was measured on hematoxylin-eosin-stained heart sections using Adobe Photoshop. A minimum of 3 distinct sections were quantified for each mouse of each genotype in a blinded manner. Placental Jz/Lb ratio was measured using FIJI (ImageJ v2.0.0, Schindelin et al., 2012) in a blinded manner. CD34 stained placental sections were digitally scanned using Aperio VERSA 200 platform in Comparative Pathology Core (CPC) at School of Veterinary Medicine at the University of Pennsylvania. Images were analyzed via Aperio Microvessel Analysis algorithm as previously described (Vrooman et al., 2020).

Statistical Analysis. Differences between two groups were evaluated using Student's t-test. For three or more groups, ordinary one-way analysis of variance (ANOVA), followed up with Tukey's multiple comparisons test, was used. Two-sided Fisher's exact test was used to compare the occurrence of the thrombi in the wild-type and *+/hIC1* placentas. All analyses were performed using GraphPad Prism software. $*P < 0.05$, $**P < 0.01$, $***P < 0.001$, $****P < 0.0001$, n.s. = not significant.

Acknowledgments

Authors would like to express gratitude to Christopher Krapp, Lisa Vrooman, Joel Rurik, Olga Smirnova, Jonathan Schug, Klaus Kaestner, and Colin Conine for their guidance on this study. This work was supported by National Institutes of Health grant GM-051279-28 and R35HL140018-05, National Institute of Arthritis and Musculoskeletal and Skin Diseases grant 5T32AR053461.

Author Contributions

S.C. and M.S.B. designed the study. S.C. and J.L.T. performed experiments and maintained mouse lines. S.K.H. generated *ΔH19* allele. S.C., D.F., J.A.E. and L.L. evaluated cardiac histology. E.A.R. and X.C. evaluated placental histology. S.C. and Y.L. analyzed RNA-seq data. S.C. and M.S.B. wrote the manuscript with input from all authors.

Competing Interests

The authors declare no competing interests.

Data Availability

RNA sequencing data are deposited in GEO database under the accession number GSE199377.

References

Abi Habib, W., Brioude, F., Azzi, S., Salem, J., Das Neves, C., Personnier, C., … Netchine, I. (2017). 11p15 ICR1 Partial Deletions Associated with IGF2/H19 DMR Hypomethylation and Silver–Russell Syndrome. *Human Mutation*. https://doi.org/10.1002/humu.23131

Aykroyd, B. R. L., Tunster, S. J., & Sferruzzi-Perri, A. N. (2022). Loss of imprinting of the Igf2-H19 ICR1 enhances placental endocrine capacity via sex-specific alterations in signalling pathways in the mouse . *Development*, *149*(1). https://doi.org/10.1242/dev.199811

Barak, Y., Hemberger, M., & Sucov, H. M. (2019). Phases and Mechanisms of Embryonic Cardiomyocyte Proliferation and Ventricular Wall Morphogenesis. *Pediatric Cardiology*, *40*(7), 1359–1366. https://doi.org/10.1007/s00246-019-02164-6

Barlow, D. P., & Bartolomei, M. S. (2014). Genomic imprinting in mammals. *Cold Spring Harbor Perspectives in Biology*. https://doi.org/10.1101/cshperspect.a018382

Begemann, M., Zirn, B., Santen, G., Wirthgen, E., Soellner, L., Büttel, H.-M., … Eggermann, T. (2015). Paternally Inherited IGF2 Mutation and Growth Restriction . *New England Journal of Medicine*, *373*(4). https://doi.org/10.1056/nejmoa1415227

Borensztein, M., Viengchareun, S., Montarras, D., Journot, L., Binart, N., Lombès, M., & Dandolo, L. (2012). Double Myod and Igf2 inactivation promotes brown adipose tissue development by increasing Prdm16 expression. *FASEB Journal*. https://doi.org/10.1096/fj.12-208496

Chang, S., & Bartolomei, M. S. (2020). Modeling human epigenetic disorders in mice: Beckwith-

484 Wiedemann syndrome and Silver-Russell syndrome. *DMM Disease Models and Mechanisms*.
485 https://doi.org/10.1242/dmm.044123
486 Chen, C. P., Chang, S. Y., Lin, C. J., Chern, S. R., Wu, P. S., Chen, S. W., … Wang, W. (2018). Prenatal
487 diagnosis of a familial 5p14.3-p14.1 deletion encompassing CDH18, CDH12, PMCHL1, PRDM9
488 and CDH10 in a fetus with congenital heart disease on prenatal ultrasound. *Taiwanese Journal of*
489 *Obstetrics and Gynecology*, *57*(5). https://doi.org/10.1016/j.tjog.2018.08.023
490 Choong, O. K., Chen, C. Y., Zhang, J., Lin, J. H., Lin, P. J., Ruan, S. C., … Hsieh, P. C. H. (2019).
491 Hypoxia-induced H19/YB-1 cascade modulates cardiac remodeling after infarction. *Theranostics*,
492 *9*(22). https://doi.org/10.7150/thno.35218
493 Conigliaro, A., Costa, V., Lo Dico, A., Saieva, L., Buccheri, S., Dieli, F., … Alessandro, R. (2015).
494 CD90+ liver cancer cells modulate endothelial cell phenotype through the release of exosomes
495 containing H19 lncRNA. *Molecular Cancer*, *14*(1), 1–11. https://doi.org/10.1186/s12943-015-0426-
496 x
497 Constância, M., Hemberger, M., Hughes, J., Dean, W., Ferguson-Smith, A., Fundele, R., … Reik, W.
498 (2002). Placental-specific IGF-II is a major modulator of placental and fetal growth. *Nature*,
499 *417*(6892), 945–948. https://doi.org/10.1038/nature00819
500 DeChiara, T. M., Robertson, E. J., & Efstratiadis, A. (1991). Parental imprinting of the mouse insulin-like
501 growth factor II gene. *Cell*. https://doi.org/10.1016/0092-8674(91)90513-X
502 Dor, Y., Camenisch, T. D., Itin, A., Fishman, G. I., McDonald, J. A., Carmeliet, P., & Keshet, E. (2001).
503 A novel role for VEGF in endocardial cushion formation and its potential contribution to congenital
504 heart defects. *Development*, *128*(9). https://doi.org/10.1242/dev.128.9.1531
505 Drewell, R. A., Brenton, J. D., Ainscough, J. F. X., Barton, S. C., Hilton, K. J., Arney, K. L., … Surani,
506 M. A. (2000). Deletion of a silencer element disrupts H19 imprinting independently of a DNA
507 methylation epigenetic switch. *Development*.
508 Eggermann, T., Buiting, K., & Temple, I. K. (2011). Clinical utility gene card for: Silver-Russell
509 syndrome. *European Journal of Human Genetics*. https://doi.org/10.1038/ejhg.2010.202

510 Eisenberg, L. M., & Markwald, R. R. (1995). Molecular regulation of atrioventricular valvuloseptal
511 morphogenesis. *Circulation Research*. https://doi.org/10.1161/01.RES.77.1.1
512 Engel, N., West, A. G., Felsenfeld, G., & Bartolomei, M. S. (2004). Antagonism between DNA
513 hypermethylation and enhancer-blocking activity at the H19 DMD is uncovered by CpG mutations.
514 *Nature Genetics*. https://doi.org/10.1038/ng1399
515 Freschi, A., Del Prete, R., Pignata, L., Cecere, F., Manfrevola, F., Mattia, M., … Cerrato, F. (2021). The
516 number of the CTCF binding sites of the H19/IGF2:IG-DMR correlates with DNA methylation and
517 expression imprinting in a humanized mouse model. *Human Molecular Genetics*, *30*(16).
518 https://doi.org/10.1093/hmg/ddab132
519 Freschi, A., Hur, S. K., Valente, F. M., Ideraabdullah, F. Y., Sparago, A., Gentile, M. T., … Cerrato, F.
520 (2018). Tissue-specific and mosaic imprinting defects underlie opposite congenital growth disorders
521 in mice. *PLoS Genetics*. https://doi.org/10.1371/journal.pgen.1007243
522 Gabory, A., Jammes, H., & Dandolo, L. (2010). The H19 locus: Role of an imprinted non-coding RNA in
523 growth and development. *BioEssays*. https://doi.org/10.1002/bies.200900170
524 Gabory, A., Ripoche, M. A., Le Digarcher, A., Watrin, F., Ziyyat, A., Forné, T., … Dandolo, L. (2009).
525 H19 acts as a trans regulator of the imprinted gene network controlling growth in mice.
526 *Development*. https://doi.org/10.1242/dev.036061
527 García-Padilla, C., Domínguez, J. N., Aránega, A. E., & Franco, D. (2019). Differential chamber-specific
528 expression and regulation of long non-coding RNAs during cardiac development. *Biochimica et*
529 *Biophysica Acta - Gene Regulatory Mechanisms*, *1862*(10), 194435.
530 https://doi.org/10.1016/j.bbagrm.2019.194435
531 Ghanim, M., Rossignol, S., Delobel, B., Irving, M., Miller, O., Devisme, L., … Vincent-Delorme, C.
532 (2013). Possible association between complex congenital heart defects and 11p15 hypomethylation
533 in three patients with severe Silver-Russell syndrome. *American Journal of Medical Genetics, Part*
534 *A*, *161*(3), 572–577. https://doi.org/10.1002/ajmg.a.35691
535 Gicquel, C., Rossignol, S., Cabrol, S., Houang, M., Steunou, V., Barbu, V., … Le Bouc, Y. (2005).

536 Epimutation of the telomeric imprinting center region on chromosome 11p15 in Silver-Russell
537 syndrome. *Nature Genetics*, *37*(9), 1003–1007. https://doi.org/10.1038/ng1629
538 Greco, S., Zaccagnini, G., Perfetti, A., Fuschi, P., Valaperta, R., Voellenkle, C., … Martelli, F. (2016).
539 Long noncoding RNA dysregulation in ischemic heart failure. *Journal of Translational Medicine*,
540 *14*(1), 1–14. https://doi.org/10.1186/s12967-016-0926-5
541 Haley, V. L., Barnes, D. J., Sandovici, I., Constancia, M., Graham, C. F., Pezzella, F., … Hassan, A. B.
542 (2012). Igf2 pathway dependency of the Trp53 developmental and tumour phenotypes. *EMBO*
543 *Molecular Medicine*. https://doi.org/10.1002/emmm.201101105
544 Han, L., Szabó, P. E., & Mann, J. R. (2010). Postnatal survival of mice with maternal duplication of distal
545 chromosome 7 induced by a Igf2/H19 imprinting control region lacking insulator function. *PLoS*
546 *Genetics*. https://doi.org/10.1371/journal.pgen.1000803
547 Harris, L. K., & Westwood, M. (2012). Biology and significance of signalling pathways activated by
548 IGF-II. *Growth Factors*, *30*(1), 1–12. https://doi.org/10.3109/08977194.2011.640325
549 Hobuß, L., Foinquinos, A., Jung, M., Kenneweg, F., Xiao, K., Wang, Y., … Thum, T. (2020). Pleiotropic
550 cardiac functions controlled by ischemia-induced lncRNA H19. *Journal of Molecular and Cellular*
551 *Cardiology*, *146*(July 2019), 43–59. https://doi.org/10.1016/j.yjmcc.2020.07.001
552 Hubert, F., Payan, S. M., & Rochais, F. (2018). FGF10 Signaling in Heart Development, Homeostasis,
553 Disease and Repair. *Frontiers in Genetics*. https://doi.org/10.3389/fgene.2018.00599
554 Hur, S. K., Freschi, A., Ideraabdullah, F., Thorvaldsen, J. L., Luense, L. J., Weller, A. H., … Bartolomei,
555 M. S. (2016). Humanized H19/Igf2 locus reveals diverged imprinting mechanism between mouse
556 and human and reflects Silver-Russell syndrome phenotypes. *Proceedings of the National Academy*
557 *of Sciences of the United States of America*. https://doi.org/10.1073/pnas.1603066113
558 Keniry, A., Oxley, D., Monnier, P., Kyba, M., Dandolo, L., Smits, G., & Reik, W. (2012). The H19
559 lincRNA is a developmental reservoir of miR-675 that suppresses growth and Igf1r. *Nature Cell*
560 *Biology*. https://doi.org/10.1038/ncb2521
561 Kochilas, L. K., Li, J., Jin, F., Buck, C. A., & Epstein, J. A. (1999). p57Kip2expression is enhanced

562 during mid-cardiac murine development and is restricted to trabecular myocardium. *Pediatric*
563 *Research*, *45*(5). https://doi.org/10.1203/00006450-199905010-00004
564 Kruithof, B. P. T., Krawitz, S. A., & Gaussin, V. (2007). Atrioventricular valve development during late
565 embryonic and postnatal stages involves condensation and extracellular matrix remodeling.
566 *Developmental Biology*, *302*(1). https://doi.org/10.1016/j.ydbio.2006.09.024
567 Lee, J. H., Gao, C., Peng, G., Greer, C., Ren, S., Wang, Y., & Xiao, X. (2011). Analysis of transcriptome
568 complexity through RNA sequencing in normal and failing murine hearts. *Circulation Research*,
569 *109*(12), 1332–1341. https://doi.org/10.1161/CIRCRESAHA.111.249433
570 Li, P., Cavallero, S., Gu, Y., Chen, T. H. P., Hughes, J., Hassan, A. B., … Sucov, H. M. (2011). IGF
571 signaling directs ventricular cardiomyocyte proliferation during embryonic heart development.
572 *Development*, *138*(9), 1795–1805. https://doi.org/10.1242/dev.054338
573 Liao, J., Zeng, T. B., Pierce, N., Tran, D. A., Singh, P., Mann, J. R., & Szabó, P. E. (2021). Prenatal
574 correction of IGF2 to rescue the growth phenotypes in mouse models of Beckwith-Wiedemann and
575 Silver-Russell syndromes. *Cell Reports*, *34*(6). https://doi.org/10.1016/j.celrep.2021.108729
576 Marsh, B., & Blelloch, R. (2020). Single nuclei RNA-seq of mouse placental labyrinth development.
577 *ELife*, *9*. https://doi.org/10.7554/eLife.60266
578 Maslen, C. L. (2018). Recent advances in placenta-heart interactions. *Frontiers in Physiology*, *9*(JUN), 1–
579 9. https://doi.org/10.3389/fphys.2018.00735
580 Matthiesen, N. B., Henriksen, T. B., Agergaard, P., Gaynor, J. W., Bach, C. C., Hjortdal, V. E., &
581 Østergaard, J. R. (2016). Congenital Heart Defects and Indices of Placental and Fetal Growth in a
582 Nationwide Study of 924 422 Liveborn Infants. *Circulation*, *134*(20), 1546–1556.
583 https://doi.org/10.1161/CIRCULATIONAHA.116.021793
584 Mi, H., Muruganujan, A., Ebert, D., Huang, X., & Thomas, P. D. (2019). PANTHER version 14: More
585 genomes, a new PANTHER GO-slim and improvements in enrichment analysis tools. *Nucleic Acids*
586 *Research*, *47*(D1). https://doi.org/10.1093/nar/gky1038
587 Mootha, V. K., Lindgren, C. M., Eriksson, K. F., Subramanian, A., Sihag, S., Lehar, J., … Groop, L. C.

588 (2003). PGC-1α-responsive genes involved in oxidative phosphorylation are coordinately
589 downregulated in human diabetes. *Nature Genetics*, *34*(3). https://doi.org/10.1038/ng1180
590 Penny, D. J., & Vick, G. W. (2011). Ventricular septal defect. *The Lancet*, *377*(9771), 1103–1112.
591 https://doi.org/10.1016/S0140-6736(10)61339-6
592 Perez-Garcia, V., Fineberg, E., Wilson, R., Murray, A., Mazzeo, C. I., Tudor, C., … Hemberger, M.
593 (2018). Placentation defects are highly prevalent in embryonic lethal mouse mutants. *Nature*,
594 *555*(7697), 463–468. https://doi.org/10.1038/nature26002
595 Poirier, F., Chan, C. T. J., Timmons, P. M., Robertson, E. J., Evans, M. J., & Rigby, P. W. J. (1991). The
596 murine H19 gene is activated during embryonic stem cell differentiation in vitro and at the time of
597 implantation in the developing embryo. *Development*, *113*(4).
598 https://doi.org/10.1242/dev.113.4.1105
599 Rochais, F., Sturny, R., Chao, C. M., Mesbah, K., Bennett, M., Mohun, T. J., … Kelly, R. G. (2014).
600 FGF10 promotes regional foetal cardiomyocyte proliferation and adult cardiomyocyte cell-cycle re-
601 entry. *Cardiovascular Research*, *104*(3). https://doi.org/10.1093/cvr/cvu232
602 Rychik, J., Goff, D., McKay, E., Mott, A., Tian, Z., Licht, D. J., & Gaynor, J. W. (2018). Characterization
603 of the Placenta in the Newborn with Congenital Heart Disease: Distinctions Based on Type of
604 Cardiac Malformation. *Pediatric Cardiology*, *39*(6), 1165–1171. https://doi.org/10.1007/s00246-
605 018-1876-x
606 Sandovici, I., Georgopoulou, A., Pérez-García, V., Hufnagel, A., López-Tello, J., Lam, B. Y. H., …
607 Constância, M. (2022). The imprinted Igf2-Igf2r axis is critical for matching placental
608 microvasculature expansion to fetal growth. *Developmental Cell*, *57*(1), 63-79.e8.
609 https://doi.org/10.1016/j.devcel.2021.12.005
610 SanMiguel, J. M., Abramowitz, L. K., & Bartolomei, M. S. (2018). Imprinted gene dysregulation in a
611 Tet1 null mouse model is stochastic and variable in the germline and offspring. *Development*
612 *(Cambridge)*, *145*(7). https://doi.org/10.1242/dev.160622
613 Savolainen, S. M., Foley, J. F., & Elmore, S. A. (2009). Histology atlas of the developing mouse heart

with emphasis on E11.5 to E18.5. *Toxicologic Pathology*, *37*(4), 395–414. https://doi.org/10.1177/0192623309335060

Schindelin, J., Arganda-Carreras, I., Frise, E., Kaynig, V., Longair, M., Pietzsch, T., … Cardona, A. (2012). Fiji: An open-source platform for biological-image analysis. *Nature Methods*. https://doi.org/10.1038/nmeth.2019

Serra, A., Eirich, K., Winkler, A. K., Mrasek, K., Ghring, G., Barbi, G., … Schindler, D. (2012). Shared copy number variation in simultaneous nephroblastoma and neuroblastoma due to Fanconi anemia. *Molecular Syndromology*, *3*(3), 120–130. https://doi.org/10.1159/000341935

Shen, H., Cavallero, S., Estrada, K. D., Sandovici, I., Kumar, S. R., Makita, T., … Sucov, H. M. (2015). Extracardiac control of embryonic cardiomyocyte proliferation and ventricular wall expansion. *Cardiovascular Research*, *105*(3), 271–278. https://doi.org/10.1093/cvr/cvu269

Shen, H., Gan, P., Wang, K., Darehzereshki, A., Wang, K., Ram Kumar, S., … Sucov, H. M. (2020). Mononuclear diploid cardiomyocytes support neonatal mouse heart regeneration in response to paracrine IGF2 signaling. *ELife*, *9*, 1–24. https://doi.org/10.7554/eLife.53071

Sibley, C. P., Coan, P. M., Dean, W., Hughes, J., Smith, P., Reik, W., & Burton, G. J. (2004). Regulates the Diffusional Exchange Characteristics of the Mouse Placenta, *2*.

Snider, P., & Conway, S. J. (2011). *Probing human cardiovascular congenital disease using transgenic mouse models*. *Progress in Molecular Biology and Translational Science* (1st ed., Vol. 100). Elsevier Inc. https://doi.org/10.1016/B978-0-12-384878-9.00003-0

Soellner, L., Kraft, F., Sauer, S., Begemann, M., Kurth, I., Elbracht, M., & Eggermann, T. (2019). Search for cis-acting factors and maternal effect variants in Silver-Russell patients with ICR1 hypomethylation and their mothers. *European Journal of Human Genetics*, *27*(1). https://doi.org/10.1038/s41431-018-0269-1

Soemedi, R., Wilson, I. J., Bentham, J., Darlay, R., Töpf, A., Zelenika, D., … Keavney, B. D. (2012). Contribution of global rare copy-number variants to the risk of sporadic congenital heart disease. *American Journal of Human Genetics*, *91*(3). https://doi.org/10.1016/j.ajhg.2012.08.003

640 Spicer, D. E., Hsu, H. H., Co-Vu, J., Anderson, R. H., & Fricker, F. J. (2014). Ventricular septal defect.
641 *Orphanet Journal of Rare Diseases*, *9*, 144. https://doi.org/10.1186/s13023-014-0144-2
642 Subramanian, A., Tamayo, P., Mootha, V. K., Mukherjee, S., Ebert, B. L., Gillette, M. A., … Mesirov, J.
643 P. (2005). Gene set enrichment analysis: A knowledge-based approach for interpreting genome-wide
644 expression profiles. *Proceedings of the National Academy of Sciences of the United States of*
645 *America*, *102*(43). https://doi.org/10.1073/pnas.0506580102
646 Sullivan, K. E., & Black, L. D. (2013). The role of cardiac fibroblasts in extracellular matrix-mediated
647 signaling during normal and pathological cardiac development. *Journal of Biomechanical*
648 *Engineering*, *135*(7). https://doi.org/10.1115/1.4024349
649 Thorvaldsen, J. L., Fedoriw, A. M., Nguyen, S., & Bartolomei, M. S. (2006). Developmental Profile of
650 H19 Differentially Methylated Domain (DMD) Deletion Alleles Reveals Multiple Roles of the
651 DMD in Regulating Allelic Expression and DNA Methylation at the Imprinted H19/Igf2 Locus.
652 *Molecular and Cellular Biology*. https://doi.org/10.1128/mcb.26.4.1245-1258.2006
653 Thorvaldsen, J. L., Mann, M. R. W., Nwoko, O., Duran, K. L., & Bartolomei, M. S. (2002). Analysis of
654 Sequence Upstream of the Endogenous H19 Gene Reveals Elements Both Essential and Dispensable
655 for Imprinting. *Molecular and Cellular Biology*. https://doi.org/10.1128/mcb.22.8.2450-2462.2002
656 Ueno, M., Lee, L. K., Chhabra, A., Kim, Y. J., Sasidharan, R., VanHandel, B., … Mikkola, H. K. A.
657 (2013). C-Met-Dependent Multipotent Labyrinth Trophoblast Progenitors Establish Placental
658 Exchange Interface. *Developmental Cell*, *27*(4), 373–386.
659 https://doi.org/10.1016/j.devcel.2013.10.019
660 Vega-Hernández, M., Kovacs, A., de Langhe, S., & Ornitz, D. M. (2011). FGF10/FGFR2b signaling is
661 essential for cardiac fibroblast development and growth of the myocardium. *Development*, *138*(15).
662 https://doi.org/10.1242/dev.064410
663 Von Gise, A., & Pu, W. T. (2012). Endocardial and epicardial epithelial to mesenchymal transitions in
664 heart development and disease. *Circulation Research*, *110*(12), 1628–1645.
665 https://doi.org/10.1161/CIRCRESAHA.111.259960

666 Vrooman, L. A., Rhon-Calderon, E. A., Chao, O. Y., Nguyen, D. K., Narapareddy, L., Dahiya, A. K., …
667 Bartolomei, M. S. (2020). Assisted reproductive technologies induce temporally specific placental
668 defects and the preeclampsia risk marker sFLT1 in mouse. *Development (Cambridge, England)*,
669 *147*(11). https://doi.org/10.1242/dev.186551
670 Wakeling, E. L., Brioude, F., Lokulo-Sodipe, O., O'Connell, S. M., Salem, J., Bliek, J., … Netchine, I.
671 (2017). Diagnosis and management of Silver-Russell syndrome: First international consensus
672 statement. *Nature Reviews Endocrinology*, *13*(2), 105–124. https://doi.org/10.1038/nrendo.2016.138
673 Wang, Y., Sun, X., & Sun, X. (2021). The Functions of LncRNA H19 in the Heart. *Heart Lung and*
674 *Circulation*. https://doi.org/10.1016/j.hlc.2021.10.022
675 Woods, L., Perez-Garcia, V., & Hemberger, M. (2018). Regulation of Placental Development and Its
676 Impact on Fetal Growth—New Insights From Mouse Models. *Frontiers in Endocrinology*,
677 *9*(September), 1–18. https://doi.org/10.3389/fendo.2018.00570
678

679 **Supplemental Information**

680 **Generation of *ΔH19* allele.** Two pairs of gRNA targeting the *H19* gene are listed in Supplemental Table
681 1. gRNA was prepared following a protocol from Yang et al. (Yang, Wang, & Jaenisch, 2014) with
682 modifications. px335 plasmid (Addgene, Watertown, MA) was PCR amplified using Phusion high-
683 fidelity DNA polymerase (New England Biolabs, Ipswich, MA) and the primer set listed in Supplemental
684 Table 1. ~117bp PCR product was gel-purified using the Gel Extraction kit (Qiagen, Hilden, Germany)
685 according to the manufacturer's instruction. Using the gel-purified product as template, *in vitro*
686 transcription of gRNA was setup using T7 High Yield RNA Synthesis kit (New England Biolabs)
687 according to manufacturer's instructions. Transcribed gRNA was purified using the MEGAclear kit (Life
688 Technologies, Carlsbad, CA) according to manufacturer's instructions. 50ng/µl left and right sgRNA
689 together with 100ng/µl Cas9 mRNA was injected per zygote stage embryo by the Transgenic and
690 Chimeric Mouse Facility at the University of Pennsylvania. The targeted allele was validated using
691 Southern blot as previously described (Joanne L. Thorvaldsen, Duran, & Bartolomei, 1998) and PCR and
692 sequencing across junctions of *ΔH19* alleles. Obtained chimeras and germ line transmission animals were
693 PCR-genotyped for the *ΔH19* allele using primers (Supplemental Table 1).

694

695 **Genotyping.** Mouse genomic DNA for PCR genotyping was isolated from each animal as previously
696 described (SanMiguel, Abramowitz, & Bartolomei, 2018). Primers used for sex genotyping and
697 genotyping of *hIC1, ΔH19* and *Δ3.8* alleles are listed in Supplemental Table 1. For all genotypes, the
698 maternal allele is listed first and the paternal allele second.

699 **RNA Sequencing library preparation and analysis.** E12.5 hearts were lysed with Collagenase (Sigma-
700 Aldrich), Dispase II (Sigma-Aldrich), and DNase I (Sigma-Aldrich). Cardiac endothelial cells were
701 collected using MACS CD31 microbeads (Miltenyi Biotec, Bergisch Gladbach, Germany) and RNA was
702 isolated using RNeasy Micro kit (Qiagen). After confirming RNA integrity using Bioanalyzer (Agilent
703 Technologies, Santa Clara, CA), mRNA library was generated from 25ng RNA using NEBNext Poly(A)
704 mRNA Magnetic Isolation Module and Ultra II RNA Library Prep Kit (New England Biolabs). Library
705 quality was assessed by Bioanalyzer (Agilent Technologies) and TapeStation (Agilent Technologies).
706 Sequencing was performed on NovaSeq 6000 (Illumina, San Diego, CA). Quality of raw fastq reads was
707 assessed using FastQC version 0.11.5 (Andrews, Krueger, Seconds-Pichon, Biggins, & Wingett, 2015).
708 Reads were aligned to the GRCm38/mm10 reference using STAR version 2.4.0i with default parameters
709 and maximum fragment size of 2000 bp (Dobin et al., 2013). Properly paired primary alignments were
710 retained for downstream analysis using Samtools version 1.9. Count matrices were generated using
711 FeatureCounts version 1.6.2 against RefSeq gene annotation and read into DESeq2 (Love, Huber, &
712 Anders, 2014) to perform normalization and statistical analysis.
713
714 **Supplemental Figure 1. Serial cross-sections of E15.5 *+/hIC1* embryonic heart with BPV.**
715 Sequential histological sections demonstrating the bicuspid pulmonary valve (BPV) phenotype.
716 Rudimentary anterior cusp can be seen fused with the right pulmonary cusp (raphe) in sections denoted
717 by * above the valve.
718
719 **Supplemental Figure 2. Supplementary data for anomalies observed in +/*hIC1* placentas.**
720 (A) Fetal to placental weight ratios of the wild-type (blue) and *+/hIC1* (red) samples at E11.5, E12.5,
721 E14.5 and E15.5. Each data point represents an average ratio of each genotype from one litter. (B)
722 Example of labyrinth zones that were used to quantify the microvessel density in CD34 immunostained
723 E17.5 wild-type and *+/hIC1* placental sections from Figure 3G. Thrombi in *+/hIC1* placentas were
724 excluded. Scale bars = 1mm. Statistics used are (A) multiple unpaired t-tests; ns = not significant.
725
726 **Supplemental Figure 3. Characterization of *⊿H19* allele.**
727 (A) Targeting strategy to generate the *⊿H19* allele. The endogenous *H19* locus is shown with restriction
728 sites, gRNA locations used to generate the deletion and binding sites for probes used in Southern blot
729 analysis (thick lines). (B) Southern blot analysis of *⊿H19* allele. Founder 4131 line was generated using

730 gRNA pair A, and founder 4133 line was generated using gRNA pair B (Supplemental Table 1). 3' probe
731 and 5' probe were hybridized to XbaI- and KpnI-digested DNA, respectively. The sizes of the DNA
732 fragments are shown on the right. (C) Allele-specific *Igf2* expression in wild-type and *⊿H19/+* neonatal
733 tongue, heart and liver analyzed by restriction fragment length polymorphism (RFLP). Ladder, genotypes
734 and c (*Mus castaneus*, paternal) and b (C57BL/6, maternal) allele controls are indicated above each gel.
735 Quantification of band densitometry is shown below each gel, with percent of maternal allele expression
736 relative to paternal allele indicated. No expression from the maternal *Igf2* allele was observed in liver. (D)
737 Neonatal body weight of *⊿H19/+* and *+/⊿H19* pups at postnatal day 0 (mean ± SD). Unpaired Student's t-
738 test; ****$P < 0.0001$, ns = not significant.
739

740 **Supplemental Figure 4. Supplementary data for rescue upon maternal *⊿H19* transmission.**
741 (A) Ratio of wild-type, *⊿H19/+, +/hIC1* and *⊿H19/hIC1* embryos observed in E11.5 and E17.5 litters (>5
742 pups). Each data point represents one litter. (B) (Left) Relative placental weights of E17.5 wild-type,
743 *⊿H19/+, +/hIC1* and *⊿H19/hIC1* samples, normalized to the average placental weight of the wild-type
744 littermates (mean ± SD). (Right) Fetal to placental weight ratio in E17.5 wild-type, *⊿H19/+, +/hIC1* and
745 *⊿H19/hIC1* samples (mean ± SD). (C) Relative total expression of *H19* and *Igf2* in E17.5 wild-type,
746 *⊿H19/+, +/hIC1* and *⊿H19/hIC1* liver and tongue samples (mean ± SD). (B, C) Each data point
747 represents an individual conceptus from different litters. One-way ANOVA with Tukey's multiple
748 comparisons test; *$P < 0.05$, **$P < 0.01$, ***$P < 0.001$, ****$P < 0.0001$, ns = not significant.
749

750 **Supplemental Figure 5. Supplementary data for rescue upon maternal *⊿3.8* transmission.**
751 (A) (Left) Relative placental weights of E17.5 wild-type, *⊿3.8/+, +/hIC1* and *⊿3.8/hIC1* samples,
752 normalized to the average placental weight of the wild-type littermates (mean ± SD). (Right) Fetal to
753 placental weight ratio in E17.5 wild-type, *⊿3.8/+, +/hIC1* and *⊿3.8/hIC1* samples (mean ± SD). (B)
754 Relative total expression of *H19* and *Igf2* in E17.5 wild-type, *⊿3.8/+, +/hIC1* and *⊿3.8/hIC1* liver and
755 tongue samples (mean ± SD). (C) Junctional zone (Jz) to labyrinth (Lb) ratio in E17.5 wild-type, *⊿3.8/+,*
756 *+/hIC1* and *⊿3.8/hIC1* placentas. (A, B, C) Each data point represents an individual conceptus from
757 different litters. One-way ANOVA with Tukey's multiple comparisons test; *$P < 0.05$, **$P < 0.01$, ***$P <$
758 0.001, ****$P < 0.0001$, ns = not significant.
759

760 **Supplemental Figure 6. Supplementary data for differential gene expression of *+/hIC1* hearts.**
761 (A) DAPI (blue) on E17.5 wild-type and *+/hIC1* hearts from Figure 6C. Images on the right are enlarged
762 from the boxed area of images on the left. Scale bars = 100 μm. (B) Immunofluorescence staining for
763 MF20 (red), collagen I (green), and DAPI (blue) on E17.5 *+/hIC1* hearts. Images on the right are enlarged
764 from the boxed area of images on the left. Scale Bars = 100 μm. (C) Same-sex comparisons between
765 *+/hIC1* and the wild-type samples analyzed by RNA sequencing.

766

767 **Supplemental Figure 7.** (A) Volcano plot depicting comparison of *⊿H19/hIC1* and wild-type cardiac
768 endothelial cells. (B) Volcano plot depicting comparison of *+/hIC1* and *⊿H19/hIC1* cardiac endothelial
769 cells. (C) GO pathways that are enriched for 46 DEGs between *+/hIC1* and *⊿H19/hIC1* samples.
770

771 **Supplemental Figure 8.** (A) Volcano plot depicting comparison of *+/hIC1* and *⊿3.8/hIC1* cardiac
772 endothelial cells. (B) GO pathways that are enriched for 116 DEGs that are commonly differentially
773 expressed in *+/hIC1* compared to wild-type and *⊿3.8/hIC1* samples. (C) Volcano plot depicting
774 comparison of *⊿3.8/+* and wild-type cardiac endothelial cells.
775

776 **Supplemental Figure 9. Enrichment tests for BRIDEAU_IMPRINTED_GENES using GSEA.**
777 Normalized enrichment score (NES), nominal p-value, enrichment plot and expression heatmap of the
778 analyzed gene set comparing (A) *+/hIC1* and wild-type, (B) *⊿H19/+* and wild-type, (C) *⊿H19/hIC1* and
779 wild-type cardiac endothelial cells.
780

781 **Supplemental References**

782 Andrews, S., Krueger, F., Seconds-Pichon, A., Biggins, F., & Wingett, S. (2015). FastQC. A quality
783 control tool for high throughput sequence data. Babraham Bioinformatics.

784 de Waal, E., Vrooman, L. A., Fischer, E., Ord, T., Mainigi, M. A., Coutifaris, C., … Bartolomei, M. S.
785 (2015). The cumulative effect of assisted reproduction procedures on placental development and
786 epigenetic perturbations in a mouse model. *Human Molecular Genetics*.
787 https://doi.org/10.1093/hmg/ddv400

788 Dobin, A., Davis, C. A., Schlesinger, F., Drenkow, J., Zaleski, C., Jha, S., … Gingeras, T. R. (2013).
789 STAR: Ultrafast universal RNA-seq aligner. *Bioinformatics*, *29*(1).
790 https://doi.org/10.1093/bioinformatics/bts635

791 Hur, S. K., Freschi, A., Ideraabdullah, F., Thorvaldsen, J. L., Luense, L. J., Weller, A. H., … Bartolomei,
792 M. S. (2016). Humanized H19/Igf2 locus reveals diverged imprinting mechanism between mouse
793 and human and reflects Silver-Russell syndrome phenotypes. *Proceedings of the National Academy*
794 *of Sciences of the United States of America*. https://doi.org/10.1073/pnas.1603066113

Love, M. I., Huber, W., & Anders, S. (2014). Moderated estimation of fold change and dispersion for RNA-seq data with DESeq2. *Genome Biology*, *15*(12). https://doi.org/10.1186/s13059-014-0550-8

Plasschaert, R. N., & Bartolomei, M. S. (2014). Genomic imprinting in development, growth, behavior and stem cells. *Development (Cambridge)*. https://doi.org/10.1242/dev.101428

SanMiguel, J. M., Abramowitz, L. K., & Bartolomei, M. S. (2018). Imprinted gene dysregulation in a Tet1 null mouse model is stochastic and variable in the germline and offspring. *Development (Cambridge)*, *145*(7). https://doi.org/10.1242/dev.160622

Thorvaldsen, J. L., Mann, M. R. W., Nwoko, O., Duran, K. L., & Bartolomei, M. S. (2002). Analysis of Sequence Upstream of the Endogenous H19 Gene Reveals Elements Both Essential and Dispensable for Imprinting. *Molecular and Cellular Biology*. https://doi.org/10.1128/mcb.22.8.2450-2462.2002

Thorvaldsen, Joanne L., Duran, K. L., & Bartolomei, M. S. (1998). Deletion of the H19 differentially methylated domain results in loss of imprinted expression of H19 and Igf2. *Genes and Development*. https://doi.org/10.1101/gad.12.23.3693

Weaver, J. R., Susiarjo, M., & Bartolomei, M. S. (2009). Imprinting and epigenetic changes in the early embryo. *Mammalian Genome*. https://doi.org/10.1007/s00335-009-9225-2

Yang, H., Wang, H., & Jaenisch, R. (2014). Generating genetically modified mice using CRISPR/Cas-mediated genome engineering. *Nature Protocols*, *9*(8). https://doi.org/10.1038/nprot.2014.134